Master thesis report
Europhotonics Master Programme

Inter-layer functional connectivity of retinal neuronal circuits

Submission Date: 30.08.2022

Author: Anastasiia Maslianitsyna
Semester: 4
Email: anastasiia.maslianitsyna@student.kit.edu
Matriculation number: 2397888

Supervisor: Emiliano Ronzitti
Laboratory: Insitut de la Vision, Sorbonne University
KIT co-supervisor: Franco Weth
UPC co-supervisor: Artur Carnicer
Thesis dates: 01.05.22 - 31.09.22

Declaration of originality

I hereby declare that the present thesis is original work written by me alone, that I have indicated completely and precisely all aids used as well as all citations, whether changed or unchanged, of other theses and publications, and that I have observed the KIT Statutes for Upholding Good Scientific Practice, as amended. I am aware that any false claim made here results in failing the examination.

Ich versichere wahrheitsgemäß, die Arbeit selbstständig verfasst, alle benutzten Quellen und Hilfsmittel vollständig und genau angegeben und alles kenntlich gemacht zu haben, was aus Arbeiten anderer unverändert oder mit Abänderungen entnommen wurde sowie die Satzung des KIT zur Sicherung guter wissenschaftlicher Praxis in der jeweils gültigen Fassung beachtet zu haben.

Anastasiia Maslianitsyna Paris, 29.08.2022

Contents

List of Figures

List of Abbreviations

2P	Two Photon
AOD	Acousto-optic deflector
BFP	Back focal plane
CCD	Charge-coupled device
CGH	Computer Generated Holography
CMOS	Complementary metal–oxide–semiconductor
CW	Continuous Wave
DMD	Digital Micromirror Device
FFP	Front focal plane
FFT	Fast Fourier transform
FWHM	Full Width Half Maximum
GCL	Ganglion Cell Layer
GS	Gerchberg-Saxton algorithm
INL	Inner Nuclear Layer
IPL	Inner Plexiform Layer
IR	Infrared
LC	Liquid crystal

LED	Light-emitting diode
ONL	Outer Nuclear Layer
OPL	Outer Plexiform Layer
PMT	Photomultiplier Tube
RP	Retinitis Pigmentosa
SLM	Spatial Light Modulator
TF	Temporal Focusing

Abstract

Optogenetic therapy opens new horizons in treating blindness. To successfully implement it and restore vision, scientists use an ever-evolving set of physical methods that optically stimulate cells in the retina. This master thesis report presents a summary of the eye and retina functioning in view of optogenetic blindness therapy, as well as different techniques for retina illumination, including computer generated holography.

The aim of the master thesis is to enhance an optical strategy for studying the neural connections in the retina. A light modulator was successfully integrated into the set-up, and its spatial resolution was studied. This is an important step in recreating retinal functionality with optogenetics therapy.

Introduction

The number of people suffering from vision impairment is on the order of hundreds of millions, and tens of millions more are completely blind [1]. The multitude of diseases and their complex nature make it impossible to find a single cure and call for increasingly synergistic efforts between pharmacological, genetic and technological approaches to understand and treat it.

Optogenetics is a revolutionary neurobiology method that was introduced a couple of decades ago. Its central idea relies on the fact that light-sensitive proteins (called microbial opsins [2]) can be genetically expressed in neurons, making them activated or inhibited by controlling the external illumination. With this tool specific cell types can be precisely and non-invasively manipulated to study the neural circuits and their role in behaviour or alterations in pathological states, which promises to exponentially increase neuroscience's capacity to elucidate brain functioning. Apart from that, optogenetics has also offered new therapeutic opportunities for human clinical applications, especially to treat visual diseases. In particular, few millions of individuals are affected by degenerative retinal diseases in which the photoreceptors — the retinal neurons that capture the light from the visual scene — are progressively compromised. In this case an optogenetic therapy can be used to "substitute" the photoreceptors by alternative retinal cells made responsive to light.

The retina is a highly specialised and complex hub for visual computation where multiple layers of different cells process the visual signal from the photoreceptors and prepare it to go to higher visual centres in the brain (see section 1.3). Thus, it is far from trivial to just "substitute" one light-sensitive cell type for another, as their patterns of activation are physiologically different. In other words, if a given retinal cell type is made light-sensitive to by-pass the disrupted photoreceptors, then, for each visual scene we want a person to see, we need to

activate the new cells with a specific pattern of activation that would normally occur during the scene in these cells and not the one from the photoreceptors. Hence, vision restoration via a so-called 'optogenetic therapy' requires a deep understanding of the retina functionality and the connections between the different neuron types inside.

A particularly critical aspect is the precision, the speed and the spatial distribution required to illuminate the newly generated light-sensitive cells in order to restore close-to-normal visual perception. One opportunity to address this challenge is offered by holographic-based patterned illumination techniques, where the wavefront of a laser beam is modulated to create a desired light pattern that selectively activates neurons. The modulation is done by changing the amplitude or the phase of the beam. An example of the amplitude modulation is a set-up that directs the beam onto an array of small mirrors (a digital micromirror device, or DMD) that would reflect the desired pixelated pattern in one direction, and the unwanted parts in the other. Phase modulation requires a more complex device that would allow to independently control the phase of different spatial locations of the wavefront. This can be done with liquid crystals displays: the orientation of the molecules in each pixel can be controlled with an electric signal and this allows to control 'point-by-point' the phase of the incoming beam. Computer generated holography (CGH) is a technique that does precisely that; and it involves calculating how exactly to modify the phase in order to achieve a desired pattern as the beam propagates to the image plane.

The aim of this master thesis is to establish an optical strategy that would allow to study the connections between different cell layers in the retina. This will pave the way to model and to predict the correct pattern of activation of a certain cell type for a given visual scene.

I structured this report in different sections. In Chapter 1, I will present a brief description of eye anatomy and retina functioning, and then focus on the biological outlook of vision loss and optogenetic therapy for visual restoration. In Chapter 2, I will present the theoretical principles of light shaping methods and give a brief summary of their current state-of-the art and main applications. In Chapter 3, I will focus on the experimental work, describing the developed optical setup and the specific goals reached: in particular, on the spatial precision, resolution and uniformity of light patterning via DMD- and CGH illumination. I will also report

on the challenges for precise cell targeting *in vivo* and present results concerning the problem of eye movement for *in vivo* experiments. I will discuss these results and I will provide the current perspectives of the research.

Chapter 1

The eye and vision loss

1.1 Eye structure

The eye is a complex organ on the verge of both biology and optics. When we look on a visual scene, the incoming light traverses the cornea and the aqueous humour; is refracted by the lens and is finally projected onto the retina (see fig. 1.1). There, photoreceptors absorb the photons and specialised neurons relay the information to higher brain centres. In humans, retina has a characteristic invagination called a fovea: it has the highest density of photoreceptors and is responsible for high-resolution central vision.

To describe and model the eye, a useful concept is the optical axis — an imaginary line perpendicular to the surfaces of the optical elements crossed by the incoming light [3], together with the visual axis — an imaginary line that connects the fixation point (the object a person is looking at) to the fovea. Because of the eye curvature, it is convenient to use the angle subtended by optical and visual axis to express the distances on the retina. The conversion is done with the circular sector formula, $L = r\theta$, where L is the distance on the retina, $r \approx 17$ mm — the radius of the eye, and θ is the angle to the optical axis. So, from the diagram 1.1 we see the fovea is located 5^o away from the optical axis, which comes to about 1.5 mm.

Studying the eye has always been a challenge, since experiments rely on animal models and every animal is unique in this regard. Most mammals have different photoreceptors and lack the fovea [4], making mouse models difficult to compare

to humans. For a more exotic example one can look at the brown-snout spookfish that has evolved a mirror and two retinas to look up and down at the same time [5].

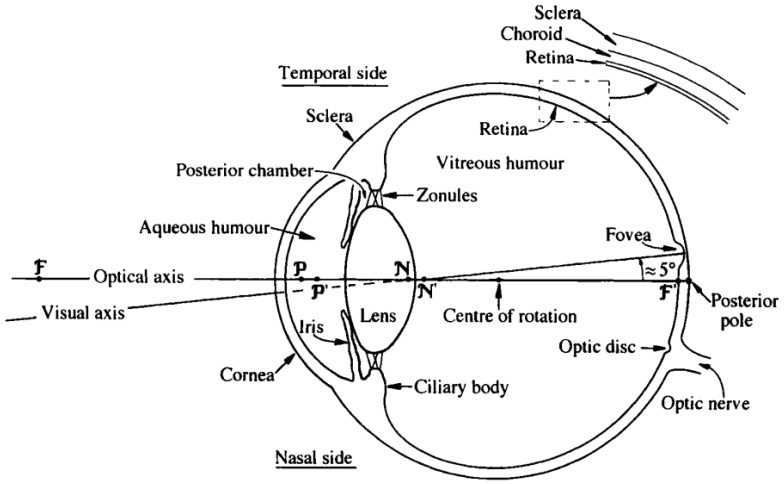

Figure 1.1: Diagram of the human right eye as seen from above [6].

1.2 Eye movements

In the context of holographic-based visual restoration, it is particularly relevant to discuss the human eye movements. The eyes have to move to keep up with the ever-changing outside world, and there are several ways this is accomplished. First come the voluntary eye movements [7]: saccades, long jumps between objects (gazing around the room, reading); smooth pursuit movements that track a moving object; and vergence moves that allow us to focus on close and distant objects. They are illustrated in the fig. 1.2. Saccades and smooth pursuits are called conjugate movements because they direct both eyes in the same direction. Vergence has to be different in the left and the right eye to converge their visual axes on the object.

Vestibulo-ocular movements compensate for the head motion by keeping the image at the same place on the retina [9]. The vestibular system carries the information about the changes in the head position and transfers them to motoneurons that produce rapid corrective eye movements and stabilise the eyes relative to the external world. The precise mechanism is still being researched [10].

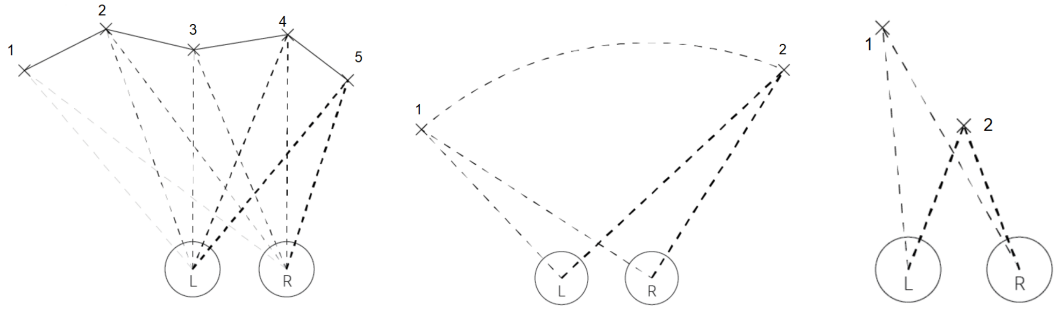

(a) A sequence of saccades. (b) Smooth pursuit motion. (c) Vergence motion.

Figure 1.2: Three types of voluntary eye movement for the left (L) and right (R) eye. Adapted from [8].

Another type of eye movement, which I further discuss in section 3.4, is the small motion done when fixating on an object. We are unaware of it, but if this motion were to be removed, our vision would fade completely because of neural adaptation [11]. For instance, most retinal ganglion cells respond primarily to transient illumination signals [12], and only weakly to constant ones. This is a challenge for the visual system, to balance the need of fixing the gaze to see the small details and the need of constantly move the photoreceptors around.

There are three types of fixational movement [13]. The first type are the microsaccades — quick single gaze jumps, like the saccades, but on a very small scale. Their amplitude typically lies between 1' and 25' (hundreds of photoreceptors), and they take around 0.01 s [14]. They are conjugate and uncontrollable, even though the mechanism of the motion is exactly the same as in large voluntary saccades.

Drift is a slow motion that occurs between microsaccades [13] and lasts around 1 s. Its amplitude is around 5', meaning that the image moves across several photoreceptors, but remains in the fovea. It isn't necessarily conjugate [14].

Tremor is a small, high-frequency motion that always accompanies the drift [13]. It is difficult to record experimentally, since with its amplitude of 30" (comparable to a diameter of a cone), it can be indistinguishable from noise [15].

The sum of these three types of fixational movement is presented in figure 1.3. It shows a trajectory of a stationary beam across a moving retina. Straight lines are the microsaccades, the slow continuous motion is the drift, and the noise-like variation is the tremor.

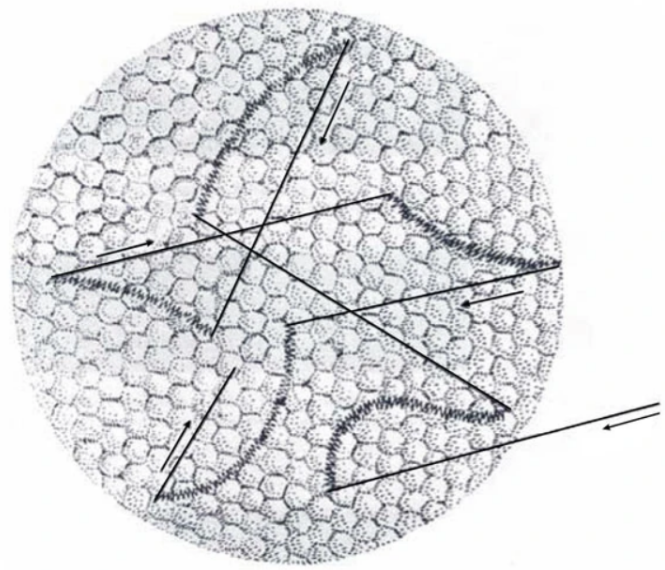

Figure 1.3: A track of a stationary beam on a retina experiencing fixational movement [16].

Nystagus is the condition of involuntary rhythmical oscillation of one or both eyes [17], which means that the patients cannot hold a steady gaze. It can be caused by many factors, but, importantly, it is prevalent in people with impaired vision. Nystagus is usually weaker in patients who lost their sight later in life [18]. Its amplitude is significantly larger than the fixation movements described above.

1.3 Retina

Retina is an intricate computational centre located in the eye. Inside of it, the information from the incoming light is conveyed to the optic nerve through many layers of specialised cells. Counter-intuitively, these layers are, in a sense, inverted, that is to say that the light has to travel through all the neuron layers before reaching the photoreceptors at the far side.

The photons are absorbed by the photoreceptors in the corresponding wavelength ranges [19]. Cones — the photoreceptors responsible for colour vision — react to blue, green and red light depending on the type of the light-sensitive protein inside of them. Blue ones account only for 10% of the total cones in the retina [20]. Rods — the night vision counterpart — react to wavelength range

between green and blue, but we do not perceive it as colour. They are great at operating in low-light conditions and they use special pathways to amplify their signal [3]. All these cells are arranged in a random mosaic across the retina [21]. Rods outnumber cones on average 20 to 1, but their densities depend on the region, which are discussed later.

The mechanism of transforming light into a neural signal — called phototransduction [22] — has only been elucidated in the twentieth century, with George Wald receiving a Nobel prize in 1967 for his "discoveries concerning the primary physiological and chemical visual processes in the eye" [23]. In a nutshell, absorption of a photon triggers a cascade of reactions that changes the flow of ions in the photoreceptor and hyperpolarises it. Hyperpolarisation means an increase in the neuron's membrane potential from the resting value of -40 mV to around -65 mV [24]. This alters the behaviour of different membrane channels, and thus the signal is transmitted to other cells.

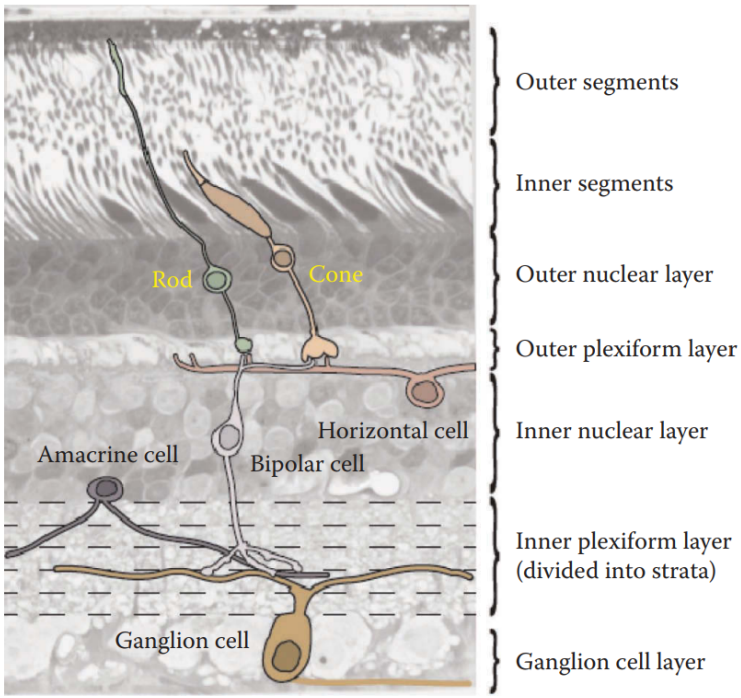

Figure 1.4: Layering of the primate retina and the position of neurons [3]. The incoming light would enter from the bottom of the diagram.

The retina is divided into nuclear layers of cell bodies and plexiform layers of connections between them [3]. Starting from the top of the diagram in fig. 1.4,

the first four layers are taken by the photoreceptors. The outer segments contain stacks of membranous disks where the transduction happens. The inner segments supply energy and synthesise transduction proteins. Photoreceptor cell bodies are in the outer nuclear layer (and, appropriately, they contain the nuclei). Finally, the photoreceptors end with an axon in the outer plexiform layer. It transmits signals to other neurons: bipolar, amacrine, and horizontal cells that are located in the inner nuclear layer. From there the signal is split up and transformed among many complex connections in the inner plexiform layer. And in the end, it reaches the ganglion cell layer — the output of the retina. The axons of the ganglion cells combine to form the optic nerve that sends the signal to the visual cortex in the brain. There, they are processed further, but this is out of the scope of this work.

The optic nerve is positioned in such a way that it needs to go through the retina to reach the brain, and that leaves no space for the photoreceptors in that particular area. This leads to the optic nerve head being a so-called blind spot. It varies slightly from person to person [25], and our brains compensate for it.

Arguably, the most important retinal region is the fovea — a 1 mm spot responsible for high acuity central vision [26]. It can be seen in fig. 1.1, situated 5^o to the temporal side from the optical axis. It dominantly contains the cones [21] that work best in bright-light conditions. It has a peculiar shape, a depression or a pit, that is best seen with an OCT (optical coherence tomography) scan. A labelled example of the fovea OCT scan is show in fig. 1.5. In the centre of the foveal pit, only the outer nuclear layer is present (which contains photoreceptors), and all the other layers with neurons and ganglion cells surround it in a ring. This leads to a peculiar transformation of the visual signal: the ganglion cells around the pit receive the signals from it as well as from the photoreceptors directly below them.

The fovea gradually gives place to the peripheral retinal regions surrounding it. There, the rods are more numerous than the cones [20]. This is why we see better contrast at night while looking slightly to the side of the object, in so-called averted vision. This technique is used to spot dim stars in the night sky with the naked eye [28].

Finally, the outermost part of the retina is the ora serrata — a 2 mm thick ring where the complex multilayer retina tissue becomes a single layer of ciliary

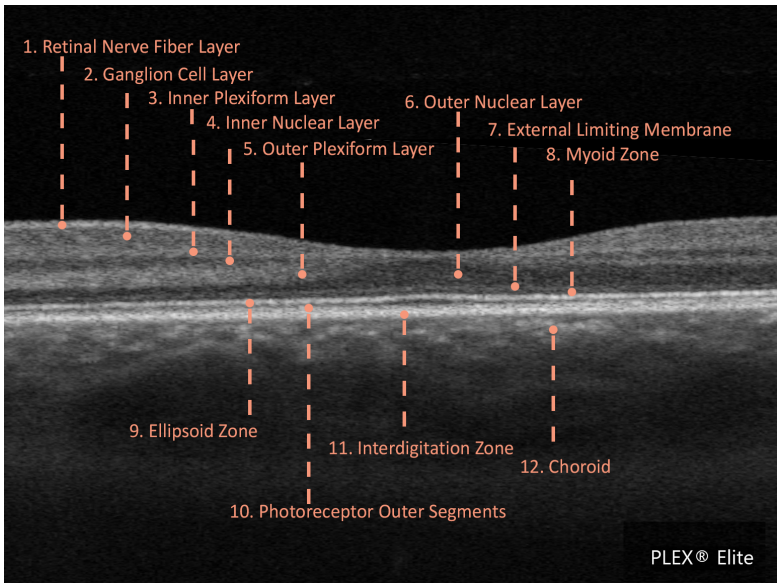

Figure 1.5: An OCT scan of the author's retina and the foveal region, labelled by the conventions from [27].

epithelium [29].

1.4 Retinal neural circuits

The retina is the brain's outpost for vision — a great part of image processing is happening in the retinal neural circuits. Scientists are still learning about the nuanced connections, since it is vital for vision loss research.

A typical neuron has a cell body (soma), several dendrites for input, and a single axon for output [3]. The foundation of any neural connection comes down to the synapses — places where two neurons touch and exchange information. The presynaptic neuron's axon sends the signal to the postsynaptic neuron's dendrite.

There are three major types of synapses. In *chemical* synapses a neuron releases small vesicles filled with a neurotrasmitter to influence the ion channels on the postsynaptic neuron's membrane. In gap junctions ions flow directly from one cell to the other through special protein tubes spanning the gap between the cells. The third type — called an ephaptic synapse — has an indirect approach: it alters the electrical potential around the postsynaptic cell [3]. This works because the neuron activates depending on the voltage across its membrane, and this volt-

age is influenced by changing either the inner or the outer electrical potential. Synapses can be sign conserving or inverting depending on whether the activation of one synapse leads to the activation of the following one or not. One cell can have many synapses all connected to a special elongated part of its axon called a ribbon [30]. For example, a dyadic synapse has two connections, and higher-order synapses can connect to more than 10 cells [31].

All these different synapses build up a network of neurons — a circuit, as seen in the fig. 1.6. The circuit unit shown in fig. 1.6b for one photoreceptor is repeated in a modular fashion across the retina.

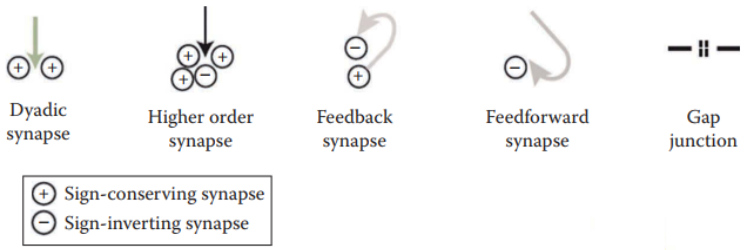

(a) Different types of synapses.

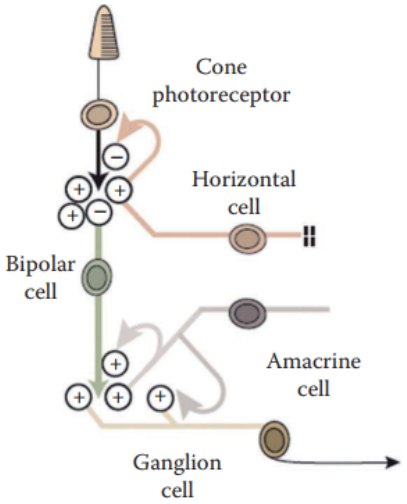

(b) A schematic circuit starting from a cone and going to a ganglion cell.

Figure 1.6: A diagram of synapses and neural circuits in the retina [3].

Now that we understand how synapses work, let us turn to the retinal neural circuits. Broadly, there are two major pathways — vertical and lateral. The vertical one fits with the intuition of conveying a signal through the layers: it starts

at the photoreceptor, goes through the bipolar cells, and ends in the ganglion cells. It is fast and simple to demonstrate; a light flash of 100 ms will trigger it. The lateral pathway, on the other hand, spreads the signal laterally in a retinal plexiform layer (since this is where all the synapses are located). In the outer plexiform layer, right after the photoreceptors, the information spreads across rods, cones and horizontal cells through gap junctions. In the inner plexiform layer the main distributors are the amacrine cells with their chemical and gap junctions. These two pathways can be seen in the fig. 1.4 by the shape of the cells' axon and dendrites — amacrine and horizontal cells have more lateral connections.

This does not mean, however, that vertical pathways carry strictly a single signal from one photoreceptor — they pool the information from many receptors using the higher-order synapses on the ribbons described above. This contributes to the compression of the information happening in the retina: about 20 rods converge on a rod bipolar cell [32], and about 100 rod bipolar cells from different rods converge on a ganglion cell [33]. This greatly helps with night vision where every photon is essential.

In the fovea the ratio of bipolar to ganglion cells is almost 1:1, enabling it to transmit much more detailed information [34]. This is an important factor for optogenetic therapy, which is concerned with finding the appropriate ganglion cell activation pattern. Upon perceiving a visual input photoreceptors activate in a certain pattern that then is progressively distorted as the signal propagates through the neuron layers. A 1:1 ratio simplifies the difference between these patterns.

Vertical and lateral pathways are antagonistic to each other; this is done to improve our perception of spatial contrast. The lateral pathway takes the signals across the retina and averages them, and this average is then subtracted from the local vertical signal. And so, the differences from the average level are amplified. This antagonistic relationship is created by negative feedback loops. For example, both horizontal and amacrine cells receive a sign-conserving signal from the photoreceptor axon and return an inverted signal through an ephaptic synapse back onto the original axon.

A final aspect of our retinal considerations is the diversity in neuronal types. All the cells we mentioned previously can be subdivided into further classes, which

specialise in analysing contrast, motion, direction, and colour. For example, a cone detecting light will activate an ON bipolar cell and deactivate an OFF bipolar cell. This way two separate channels are created for the areas of the image that are brightening (ON) and darkening (OFF).

Another example would be an AII ON amacrine cell that injects the rod signal into the cone pathway depending on the light level. Cones are handling the bright light, but for dimmer conditions rod signals flow through the same pathways that cones use. And in the dark, rod signals use only vertical pathways to avoid spreading noise laterally. So, AII cells close their gap junctions at low light levels [35].

1.5 Loss of vision

Now that we appreciate the complex multitudes of the eye, we can see in how many ways the process of vision can go wrong or even stop entirely. And, unfortunately, there indeed are many breaking points. The lens can become cloudy, in what is known as a cataract. The internal pressure can stop being maintained in a healthy range, disrupting the optic nerve — glaucoma. The retina may be left without nutrients and detach because of damage to the blood vessels as a consequence of diabetes. Each of these diseases targets a specific feature of the eye, making it impossible to find one single treatment for the loss of vision.

Relevant to this work is Retinitis Pigmentosa (RP) — a genetic disorder that gradually damages the vision, and affects 1 in 4000 people [36]. There is currently no cure for RP [37], and the researchers have identified only half of responsible gene loci. RP is divided into several stages [38], tracing the degradation of the photoreceptors: first, the rod loss leads to impaired night vision, then the periphery vision follows, after that the patients are left only with a tunnel vision, and finally they become completely blind.

Mutations are responsible for the initial loss of the rod cells — they may shorten the outer segment layer and expose the rod bodies to higher levels of oxygen than it can tolerate. Another possibility are the mutations related to calcium metabolism, which causes the cell to incorrectly open its channels and exhaust itself. This process is illustrated in the fig.1.7, where the difference in the thickness of the ONL (that contains photoreceptors) is visible between the normal

rat retina and the RP model one.

The loss of rods triggers a degradation of cones, and that is the most severe vision loss [39]. After rods die, the oxygen levels in the outer retina are increased and the cones are progressively damaged by reactive oxygen species. This is how RP develops to its most severe form.

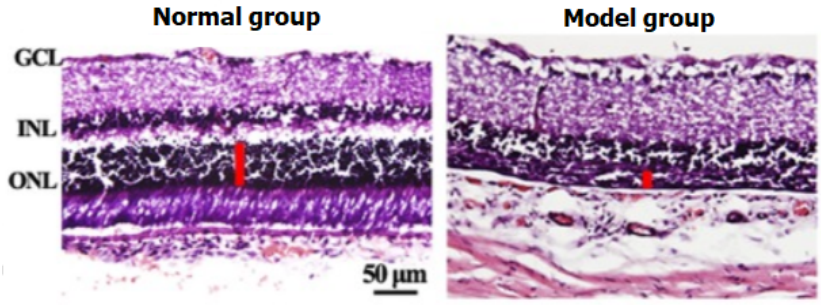

Figure 1.7: Staining images of retinal sections of rats from the model Retinitis Pigmentosa and the normal groups. ONL: outer nuclear layer; INL: inner nuclear layer; GCL: ganglion cell layer; Scale: 50 um. [40].

Chapter 2

Patterned illumination for optogenetics

2.1 Optogenetics

Being established around 2005 [41], optogenetics is an incredible tool to study and optically control the activity of neurons. It works by injecting the target cells with new DNA in order to express microbial opsins — light sensitive proteins. The injection is done with adeno-associated virus vectors [42] that are engineered to deliver the precise DNA sequence. The first discovered and expressed of these light-sensitive proteins was Channelorhodopsin-2 — a light-gated ion channel originally found in green alga [43]. Since its discovery, many modified opsins have been created to shift the excitation frequencies and achieve better photocurrents in the experiments [44].

When opsin absorbs light in a particular frequency range (with the maximum at 480 nm), its structure changes and this triggers an ion flux and a cascade of phototransduction reactions. To be more precise, the actual molecule absorbing the light is retinal — a form of vitamin A, which needs to be supplied continuously to keep the opsins operational. Luckily, the base levels of retinal in the tissue are enough for all optogenetics applications [45].

Full optical control over neurons can be achieved by using optogenetics to activate the cells and fluorescence techniques to image them [46]. A convenient method to couple with the optogenetic viral injections is calcium imaging [47].

This allows to have an optical 'read/write' interface to study neurons. Calcium imaging uses genetically encoded calcium indicators that become fluorescent when bound to Ca^{+2} — ions that are central to almost every cellular task, from metabolism to gene transcription to neural activity [48].

Optogenetics has direct implications for vision loss. Retinitis Pigmentosa causes the photoreceptors to degrade, but it spares parts of the other retinal circuitry, including the ganglion cells. This means that if we were to generate a neural signal without using the photoreceptors, the rest of the system would work just fine and the patient would be able to see something. This is where optogenetics comes in: it makes new cells sensitive to light. In this project we are targeting ganglion cells, so that after photostimulation they will start sending neural signals via the optic nerve to the brain, and thus restoring vision, albeit partially.

In a tremendous leap of technology, vision restoration with optogenetics has been achieved in 2021 [49]. By using special light-projecting goggles researchers were able to stimulate ganglion cells of an RP patient allowing him to distinguish simple objects on a white background.

2.2 Two-photon absorption

The first aspect to consider is whether to use single or two-photon processes for optogenetic stimulation of the cells. Two-photon (2p) absorption is a nonlinear phenomenon that involves a molecule absorbing two photons via a virtual state. The emission happens at a shorter wavelength because of the internal conversion processes at the top energy band. It is illustrated in fig. 2.1, along with the different laser beams needed for 1p and 2p excitation: continuous low power for 1p and pulsed high peak power for 2p.

2P fluorescence has two advantages compared to single-photon: firstly, it gives a smaller focal point because its efficiency is proportional to the square of intensity; and secondly, it uses an appropriate frequency (IR) to mitigate scattering, and so reaches deeper into the tissue [50]. Of course, it also has its disadvantages, namely in the need of more complicated experimental set-ups and pulsed lasers, but this is the price to pay for precise cell stimulation.

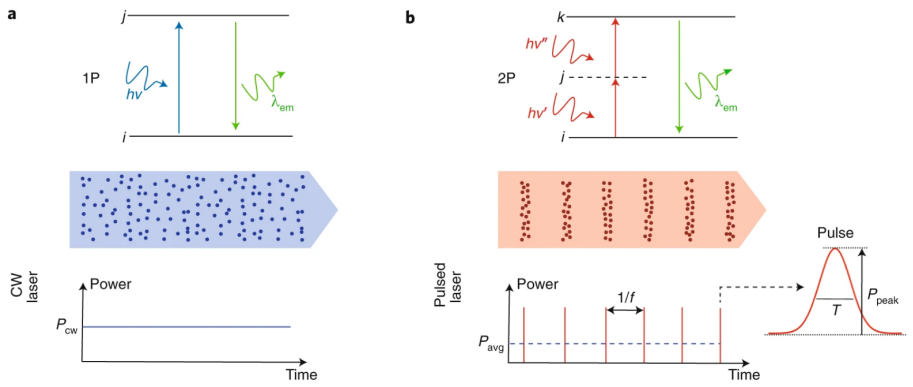

Figure 2.1: (a) Jablonski diagram for a single-photon process, and representation of the excitation beam with the power P_{CW} of a continuous-wave (CW) laser. (b) Same as a, for a two-photon process. The excitation beam in this case is pulsed with duration τ at a repetition rate f. The peak power P_{peak} of each pulse is much larger than the average power P_{avg}. From [51].

2.3 Overview of patterned stimulation methods

There are many ways to perform controlled optogenetic stimulation. As the density and the conductivity of opsins expressed in a neuron is relatively low, all of the molecules must be illuminated to trigger a neuron activation. This led to the development of different strategies, with one of them being patterned illumination. It involves creating a precise and intricate pattern of focused light in the sample plane, which excites the cells the experimenter wants. The size of neuron cell bodies can easily reach 20 um [52], while the diffraction limited spot is on the order of $\frac{\lambda}{2\mathrm{NA}} \approx 0.5$ um, so the beam can be smaller than one cell. This isn't perfect for equal and complete stimulation, so we need to circumvent this issue.

2.3.1 Scanning techniques

One solution is to use a diffraction limited spot (i.e., 0.5 um) and move it across the neuron in a scanning motion. This requires a specialised unit to deflect and offset the beam in a controllable manner. To build such a set-up you would need the scan unit itself, a scan lens, a tube lens, and an objective, arranged in a configuration shown in fig. 2.2. The scan unit plane is conjugated with the back focal plane of the objective, allowing to move the focal point in the image plane by changing the deflection angle of the scanner (thus translating angular motion

into linear). The angles for x and y movement are independent of each other and therefore require two scanners in perpendicular directions.

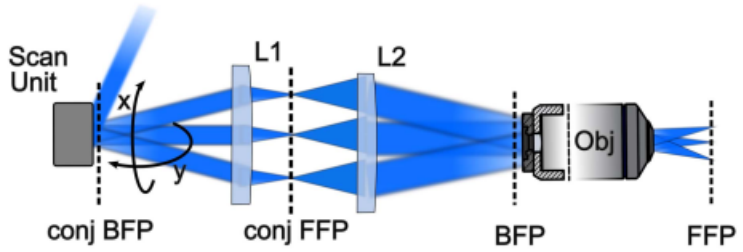

Figure 2.2: A diagram of a laser scanning setup [50]. The scan unit is able to deflect the beam in two planes (x and y), and is conjugated to the back focal plane (BFP) of the objective. L1 — scan lens, L2 — tube lens, FFP — front focal plane.

The scanning system defines how precisely we can hit the targets, at what angle and trajectory, and so determines the spatial localisation accuracy. However, the spatial resolution is not influenced by the scanning unit, since scanning the beam keeps the spot size constant. The temporal characteristics are determined partially by the time it takes to move the beam from one target to another, and also by the time needed to dwell on one target cell to induce a neural response. The latter part depends on many parameters, such as the cells and opsins used, laser power, etc [50].

A standard solution is to build a dual galvo-mirror system. Each of the mirrors is mounted on a controllable galvanometric actuator, thus allowing to deflect the beam in both x and y planes. For example, to scan the whole image the x angle is changed linearly from the minimum to the maximum value, and then one step is taken in the y angle. This is a linear scanning system, and it is different from resonant scanning, which changes the angles in a sinusoid over time. This slows down the scanning at the edges of the field of view, but allows for a much greater scanning speed overall.

An alternative approach involves acousto-optic deflectors (AODs). AODs rely on the acousto-optic effect — a change in the refractive index of a material induced by an acoustic wave passing through it [53]. Since acoustic waves are longitudinal, when they propagate perpendicular to the incoming light beam, the induced change in the refractive index looks like a diffraction grating with a

period of the sound wavelength. This virtual grating then diffracts the beam into different orders. To keep the power loss at a minimum, the light comes at the Bragg angle θ_B from the perpendicular of the sound wave's propagation to keep most of the power in the +1 order.

$$\sin(\theta_B) = \frac{\lambda}{2n\Lambda},$$

where n is the refractive index of the crystal, λ is the light wavelength, Λ — the sound wavelength [54].

Scanning techniques and their further modifications allow researchers to map functional neuronal connectivity [55], study the directional selectivity of neurons [56], and even image neuron activity in awake behaving mice [57]. The techniques are also widely used outside the neurobiology field: lidar and 3D laser scanning may use galvomirrors [58], and AODs are central to laser Q-switching [59] as well as modulating the signal for telecommunications [60].

2.3.2 Parallel techniques

Parallel modulating techniques offer an alternative approach to the patterned illumination: they sculpt the light to illuminate all neuron areas simultaneously, hence the name "parallel"; no beam scanning required. This is a major advantage of this approach — the temporal resolution is not limited by the size of the field of excitation or the number of targets (as it is in scanning), and this allows for great temporal flexibility. Of course, that is only within the limits of the minimal dwell time on one cell, which is defined by the type of opsin used.

The parallelism of this method also brings about its disadvantage — the laser power is distributed equally across the pattern. So, if we would like to excite 10 cells with a minimum power $P_{\min}$ to trigger photostimulation, we would need the beam power to be at least $10P_{\min}$. However, this does not pose a serious problem, since the peak power required for one cell is well within the range of commercially available high-power laser sources, like Ti:Sapphire [61]. For example, an action potential can be triggered in a neuron with a 1 ms 0.5 mW/um^2 pulse across a holographic spot of 15 um [62]. Also new reports have significantly improved the power throughput of these approaches [63].

To understand the two main distinctions in light modulation, we need to return to the foundations of optics and write down the complex representation of the field:

$$E(\omega, \vec{r}, t) = A(\omega, \vec{r})e^{-i\omega t + i\vec{k}\cdot\vec{r} + i\Phi(\vec{r})}$$

where A_{inc} is the amplitude of the field, and the exponent carries the phase component of a plane monochromatic wave. We can modulate the amplitude or the phase, both of which impact the light propagation.

Intensity modulation

The simplest amplitude modulation is done using an LED array. A diagram is shown in the fig. 2.3: the LED plane is conjugated to the front focal plane of the objective, where the LED pixel pattern is reproduced.

The spatial resolution is determined by the objective and the size of a single LED pixel. A typical array can be a 64x64 grid with a 20 um pixel diameter [64]. With this limited number of pixels, it makes sense to have the image of the pixel in the sample plane similar in size to a whole cell or any other region of interest: if it were too small, there wouldn't be enough pixels to cover the whole region. So, for a 64x64 array with 50 um spacing between the pixels and no magnification, the total field of excitation would be $64 \cdot 0.05 = 3.2$ by 3.2 mm.

A different set-up from the fig. 2.3 that allows to modulate many more pixels is a digital micromirror device (DMD) — an array of pixel-like mirrors that can be individually rotated ($\pm 12^o$ relative to the DMD plane). The main principle is to designate one direction of the reflected light as the "on" signal and discard everything else; this way a pixel pattern can be produced in the focal plane. The set-up is similar to the one for the LED array, but an external light source is required. To fill the whole working surface of the DMD the beam also needs to be expanded with the lenses L1 and L2.

Typical DMDs have 700-2000 pixels in each direction [65], so the field of view can be large even when one pixel is imaged as a small point (diffraction limited Airy disk). For example, a 1280x800 DMD would give a 0.512x0.32 mm field of excitation with a x40 objective [66].

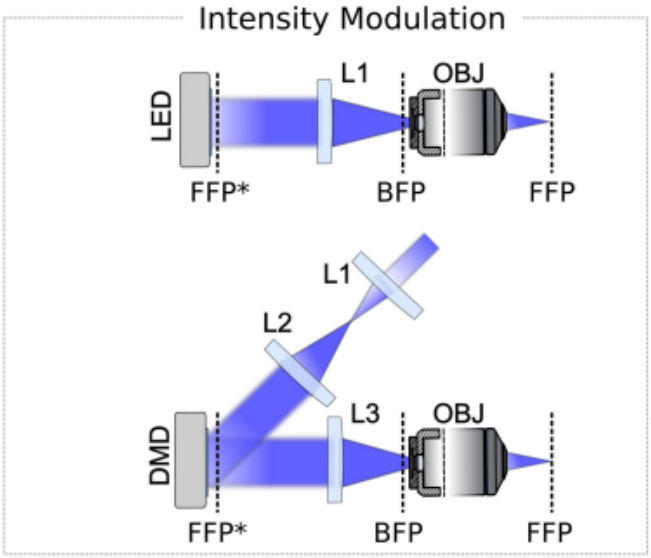

Figure 2.3: Intensity modulating techniques [50], with an LED array shown at the top, and a DMD configuration at the bottom. DMD — digital micromirror device, FFP — front focal plane, BFP — back focal plane.

Phase modulation

To understand the concept of phase modulation we need to introduce the wavefront of the field — a continuous set of all points with the same phase. Some examples are shown in the fig. 2.4. Lenses, prisms, gratings, and mirrors all modify the wavefront and change the propagation of light. However, they perform very basic modifications that are not enough for sophisticated patterned illumination.

Fraunhofer diffraction states that the field in the far field can be calculated by a Fourier transform (FT) of the original field [54]:

$$E(\omega, x, y, z, t) \propto \iint E_{\text{inc}}(\omega, x', y', 0, t) \exp\left\{-\frac{ik}{z}(x'x + y'y)\right\} \mathrm{d}x' \mathrm{d}y',$$

$$E_{\text{inc}}(\omega, x, y, 0, t) = A_{\text{inc}}(\omega, x, y) e^{-i\omega t}$$

This approximation works for the far field, i.e. for $z \gg \frac{W^2}{\lambda}$, where W is the size of the diffraction aperture. For example, with a 1 mm aperture and 1 um wavelength (IR), z should be much greater than 1 m. This is a large distance for any practical set-up. Luckily, optical lenses have a property of reproducing a

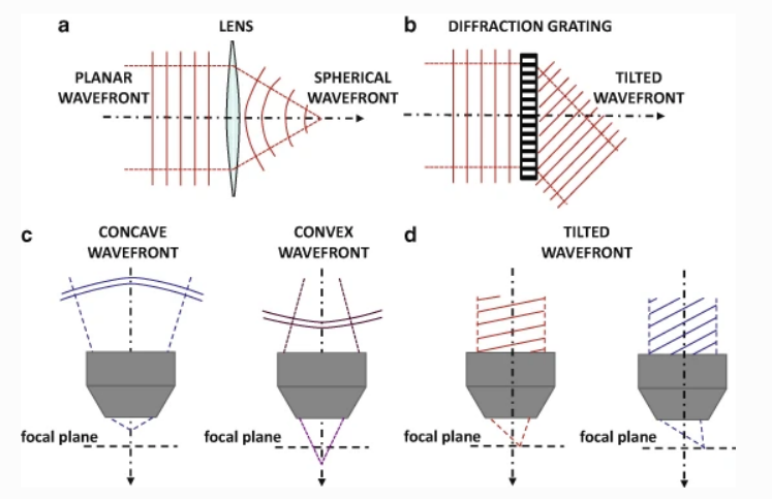

Figure 2.4: Examples of different wavefronts and their influence on light propagation. (a) A lens transforms a plane wave into a spherical one. (b) A diffraction grating tilts the wavefront in the direction of the given diffraction order. (c) Curved wavefronts affect the axial position of the focal point. For example, moving a point source away from the lens defocuses the image. (d) Combining a tilted wavefront and a lens results in the lateral shift of the focal point. Adapted from [67].

Fraunhofer diffraction pattern in their focal plane [68].

We can see that by modifying E_{inc} we can change the resulting field. To have a full control of the resulting field we need to modify both the amplitude and the phase, since there is a strict one-to-one correspondence between the functions in the FT. However, in the experiments we are using intensity $I \propto |E|^2$ (since opsins react to the number of photons), and it carries no phase information. So, we can aim to get only required amplitude A in the sample plane, and not the whole complex field E. This gives us the freedom to modify only the phase of the incoming beam.

A device that allows to control the phase of the beam point-by-point is called a liquid crystal spatial light modulator (LC-SLM, or simply SLM). The pixels are made out of twisted nematic LC molecules, which are birefringent: a wave passing through them will experience a different refractive index depending on the direction of propagation [54]. The LC molecules themselves can be rotated by applying an electric field through transparent electrodes. Therefore, a stationary incoming wave will propagate with a different n depending on the signal on the

electrodes. A plane wave will have a phase shift of $e^{ik\Delta nd}$, where k is the wave vector, Δn is the difference of the refractive indices in two LC configurations, and d is the total distance travelled in the LC.

The type of LC determines the speed of molecule reorientation and, along with the LC thickness and the voltage signal, ultimately defines the refresh rate of the SLM [69]. Typical values are on the order of 100 Hz [70, 71].

LC-SLMs are used in a variety of optical set-ups, from holographic optical tweezers [72] to digital data storage [73]. Using their birefringence property and a couple of polarisers even allows for amplitude modulation. However, let us discuss an SLM based technique particularly relevant to this project.

Computer generated holography (CGH) is a patterned illumination technique that uses an SLM to modify the phase of the light in the back focal plane. The basic set-up is shown in the fig. 2.5. A laser beam is expanded with lenses L1 and L2 onto the surface of the SLM, which is conjugated with the BFP of the objective. The inset in the figure shows the target pattern, the SLM phase mask in the BFP, and the resulting pattern in the FFP.

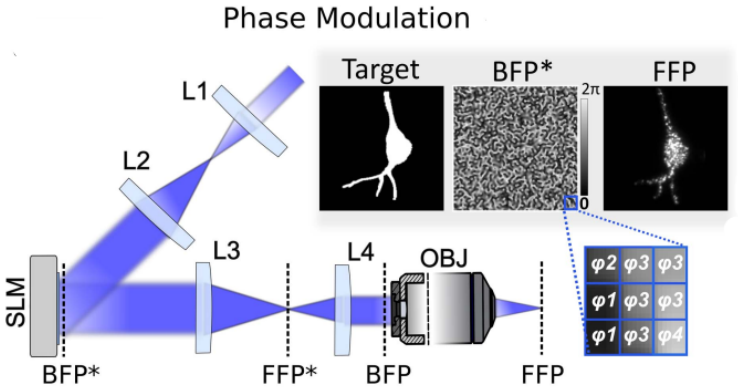

Figure 2.5: Computer generated holography set-up [50].

The crucial step in this technique is to determine the phase profile for the SLM at the back focal plane. It can be solved computationally, and many algorithms have been developed to generate phase masks that result in 2D or 3D light patterns of choice, with varying degress of efficiency, uniformity, and symmetry [74]. A simple approach was already hinted at in the fig. 2.4 (d): a lens focuses a uniformly tilted wavefront into a laterally shifted point. So, to create a pattern we would

need to get a superposition of all the waves with the tilted wavefronts that will form the image when focused.

However, experiments with cell photostimulation require a better algorithm, one that does not deal only with separate diffraction-limited light spots, but with arbitrary shapes of the illumination. Above we discussed how wave propagation can be expressed as an FT of the field, and how phase modulation can alter the intensity in the sample plane. Unfortunately, calculating a phase mask for the modulation is not as straight forward as taking an inverse FT of the desired pattern: an inverse FT would result in a complex field with the amplitude and the phase completely different from the incoming one. A single SLM modifies only the phase; we could add an amplitude modulating device to the set-up, but it would introduce additional power losses. A solution to this is the Gerchberg-Saxton (GS) algorithm [75]. It is an iterative process that optimises for the amplitude of the pattern in the sample plane, and not its phase. The phase does not influence cell photostimulation, so this works perfectly in the experiments.

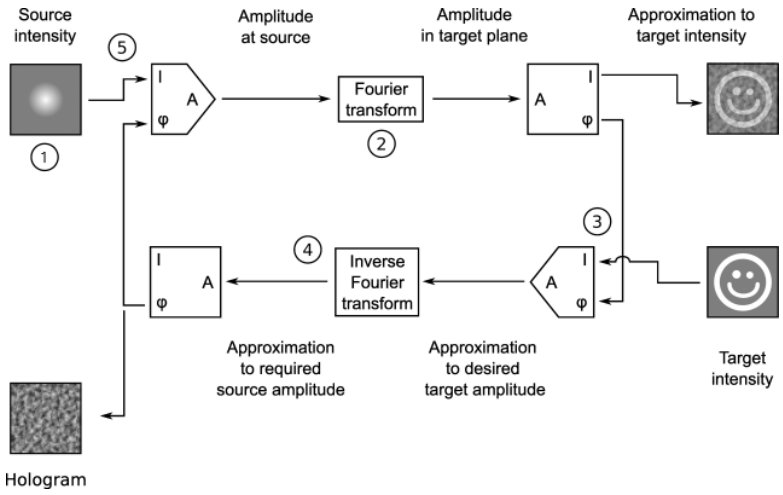

Figure 2.6: Gerchberg–Saxton algorithm for calculating the phase pattern for the SLM [76].

A diagram is laid out in the fig. 2.6. At the start of GS algorithm, we measure the source intensity (the beam coming to the SLM). Then, we generate a random phase distribution between π and $-\pi$ as the initial guess for the phase mask. This random phase is combined with the source intensity into a single complex array, on which FFT is performed (step 2). It results in a different complex array that we

split into the amplitude and the phase. The amplitude certainly will not match the target intensity (the pattern) on the first try, so we discard it and simply substitute the target intensity into the array (step 3) to let the algorithm iterate it. After an IFFT (step 4) we get an approximation of our original source field with a new phase. The source intensity is substituted instead of the approximating one (step 5), and the process repeats. After the difference between the real target intensity and its approximation becomes negligible, we stop the process and save the obtained source phase as the SLM mask (we assume that the beam falling on the SLM is a plane wave with constant phase).

An initial random phase distribution is used for better convergence compared to a constant phase [75]. The solution is not unique since a constant phase shift or a complex conjugation (for centrosymmetric intensities) would produce the same phase mask, but this is acceptable for real-life applications. The algorithm converges quickly, after around 8 iterations [77].

An example of the SLM phase mask is presented in the fig. 2.7, along with a 40 um diameter holographic spot it produces in the sample plane. A speckle pattern (non-uniform intensity) is clearly visible in the spot, and this problem is discussed more in section 3.2.

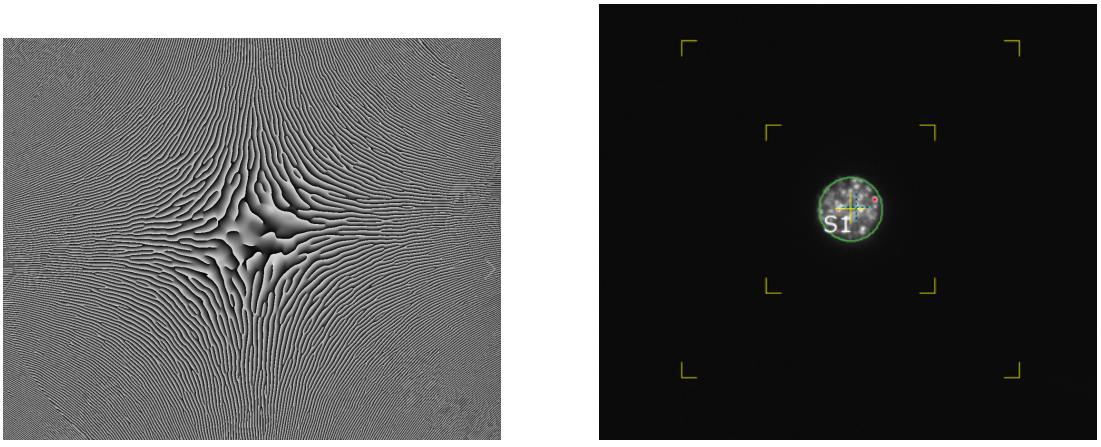

(a) (b)

Figure 2.7: An example of a SLM mask and the holographic spot (40 um) it produces in the sample plane. The border and guiding marks are for reference.

Now that we understand how CGH works, we need to consider its resolution. The theoretical resolution is defined as the size of the diffraction-limited spot

generated at the front focal plane of the objective, which is determined by the numerical aperture (NA) of the objective. Specifically, if the back aperture of the objective is completely filled by the holographic beam of wavelength λ, the Abbe limit applies [54]:

$$x_{\min} = y_{\min} = \frac{0.61\lambda}{\mathrm{NA}},$$
$$z_{\min} = \frac{2\lambda n}{\mathrm{NA}^2}$$

If the objective is underfilled with a beam of radius r, the resolution depends on the focal length, $\mathrm{NA} = f_{\mathrm{obj}}/r$.

One problem of CGH is the fact that the axial resolution worsens with the large pattern size [77], and this severely limits the accessible area in the sample. A better axial resolution would allow experiments on dense biological samples, where the cells from above and below the focal plane can accidentally activate and contribute noise.

2.4 Temporal Focusing

Temporal focusing (TF) is an additional technique that allows to improve the axial resolution of the holograms. It was proposed in 2005 [78] as an alternative to scanning imaging techniques like confocal microscopy.

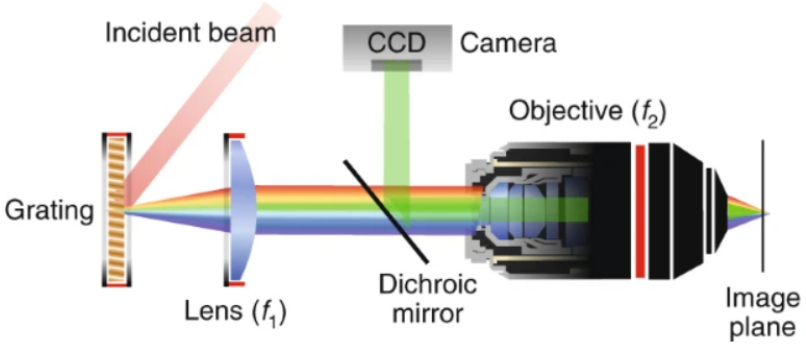

Figure 2.8: A diagram illustrating the main principle behind temporal focusing. From [51]

TF uses a short and spatially wide pulse, which hits a diffraction grating and gets dispersed into colours (see fig. 2.8). Then it goes through a telescope system

(a lens and an objective), so that the grating and the image plane are conjugated. For any intermediate point between those planes, the pulse is broadened because different spectral components have different optical paths. When it arrives at the image plane, all components come in phase and the pulse duration is restored to the original it had on the grating. Since two-photon processes reply on the square of the intensity, they will be most active only in vicinity of the focal plane ($\sim$ 5 um [79]), thus greatly improving the axial resolution.

The main drawback is the power loss on the diffraction grating — it can reach up to 20% [67]. This, combined with the high power required for parallel techniques in general, limits the maximum number of targets.

Chapter 3

Experimental part

3.1 The experimental set-up

The system used in this work allows for full optical control of the neurons, with CGH stimulation and calcium imaging (see fig. 3.1).

The CGH path is shown in red: a femtosecond pulsed beam sent by a fibre amplifier system (Satsuma Amplitude, 1030 nm, 10 W, 200 fs pulses at 1 MHz) is expanded with a telescope to fill the surface of the SLM (SLM; X10468-07, Hamamatsu Photonics). Then it hits a diffraction grating for the TF enabled or, alternatively, skips the grating with a movable mirror and goes straight to the objective for the TF disabled. With additional lenses the SLM is conjugated to the back focal plane of the objective (Zeiss, x20, NA = 1.0, water immersion), and the grating to the sample plane. The maximum power achieved at the sample plane was 1 W.

Imaging is done with a Ti:sapphire laser (Axon 920 Coherent, 920 nm, 1 W, 150 fs pulses at 80 MHz) in 2P mode. The laser beam is directed onto a pair of galvo-mirrors that allow to scan the sample in both directions in two different regimes: regular and resonant scanning. The imaging frame rate depends on the resolution: a 256x256 px image updates at 5.1 Hz, 128x128 px at 15 Hz. The resonant scanner is set at 256x256 and operates at 40 Hz.

The sample fluorescence signal is collected by the objective and transmitted with a dichroic mirror to the imaging pathway. There, with a movable mirror the light is directed onto a PMT with a chosen filter set, or to a widefield CCD

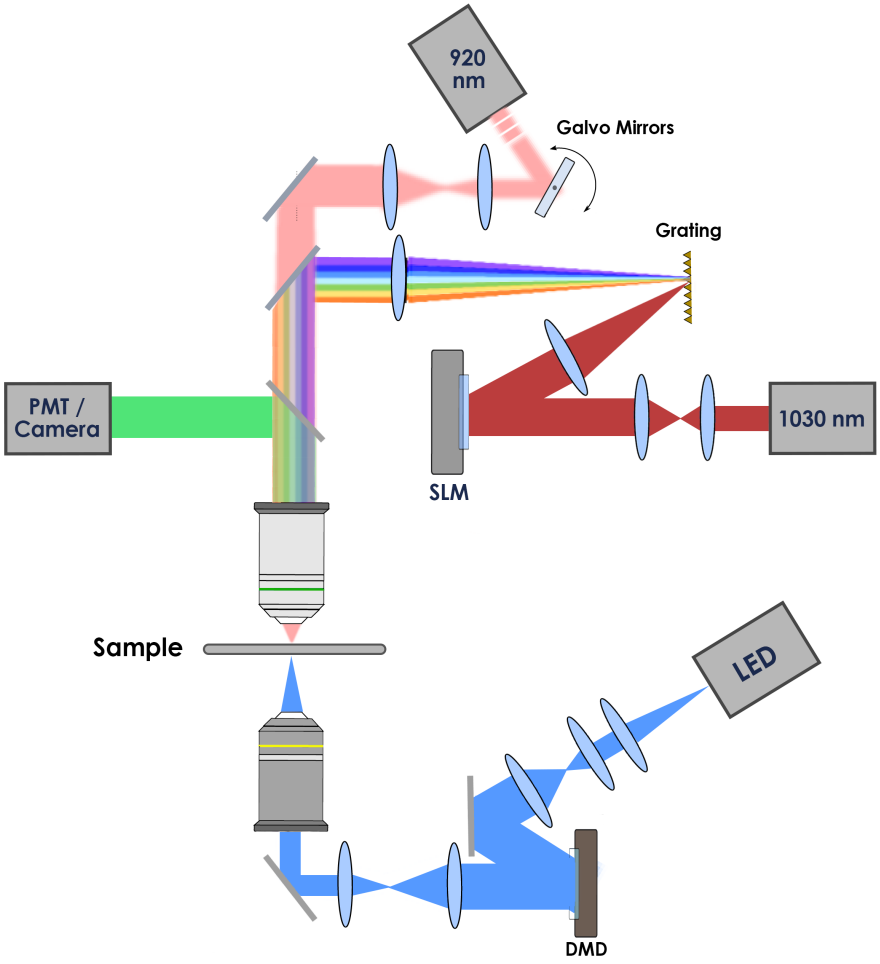

Figure 3.1: The experimental set-up showing the main four optical paths: CGH, scanning, DMD, and camera.

camera (CoolSNAP, Photometrics).

Finally, the DMD path is shown in blue. It starts with a 430 nm LED that is expanded onto the surface of the DMD (Vialux-7000, 1024x768 pixels). There, the computer controls the micromirror pattern, and their reflected light is telescoped onto the substage objective (Olympus, 10x, NA = 0.25). The light is transmitted onto the sample plane from below. The alignment and the calculations for this path are presented in the section 3.3, as they were a big part of my project.

3.2 System characterisation

In order to characterise the system performances, we generated holographic spots onto uniform um-thick fluorescent (Rhodamine-6G) layers. First, I determined the targeting location accuracy. For that we exploited the photobleaching effect — a irreversible change in the fluorescent proteins that stops them from emitting a signal. It happens when we send a very intense laser beam, and after the photobleaching it leaves a dark spot (see fig. 3.2. We initially created a pattern (for example, 3 spots with set coordinates) using the holography control panel, and kept it up to induce photobleaching in those locations. We then detected their precise positions by scanning the 920 nm imaging beam onto the sample and acquiring the signal with the PMT. This way we calibrated the hologram coordinates with the imaging coordinates.

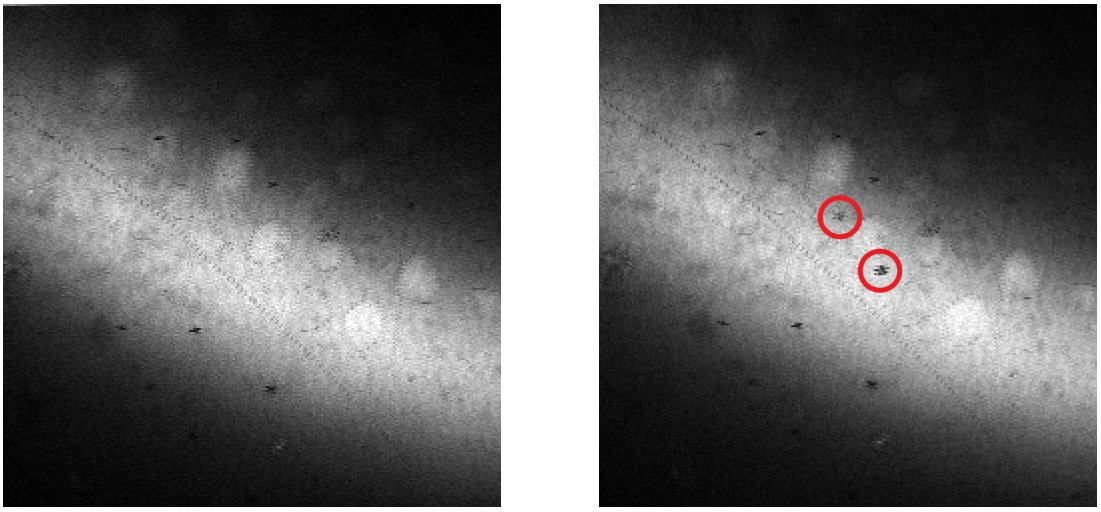

(a) (b)

Figure 3.2: Fluorescent scanning images of a Rhodamine-6G slide. (a) before photobleaching, (b) — after, with spots marked.

Next, I measured the holographic optical resolution. There are two kinds of resolution: lateral and axial. Lateral resolution is the minimal size of the spot in the sample plane. Axial resolution is the FWHM of a spot across several z (vertical) planes. I measured the axial resolution of the holography laser by recording z-stacks of a circle pattern in the focal plane, done by an automatically moving objective. I set steps of 1 um around the focal plane with a total range

of 200 um.

An image of the holographic circles is shown in fig. 3.3. It can be noted that their outline is sharp, but the intensity varies inside. These random static intensity fluctuations are called speckles, and they appear due the randomness of the phase of the beam [80]. They are caused by the Gerchberg-Saxton algorithm: it leaves the phase in the sample plane as a free parameter to be able to find the SLM phase mask. Because of that, the light fields coming from two neighbouring pixels have a random phase shift, and their interference creates a speckle pattern [81]. There are several methods to improve how homogeneous the intensity is, for example by using an incoherent light source [82] or by using a spatially sparse pattern [83] to reduce the interference. For our applications, this level of speckles is not a problem during the experiments: opsins usually diffuse along the cell membrane, thus averaging the illumination they receive.

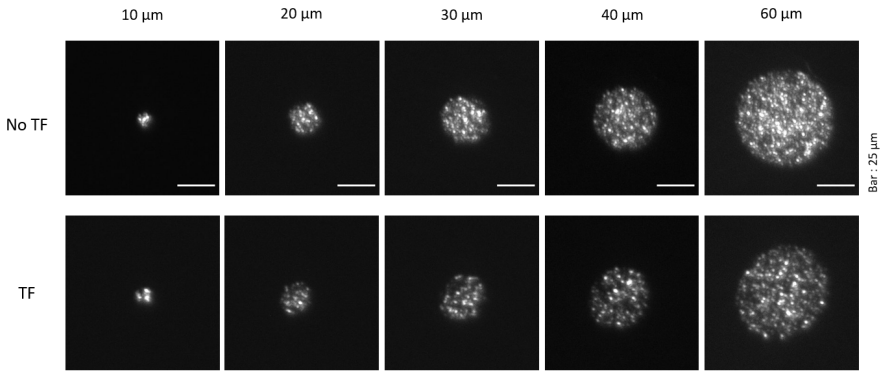

Figure 3.3: Different circle sizes as seen in the focal plane. The scale bar is 10 um. TF - temporal focusing.

To estimate the spot axial resolution, I averaged the intensity across a region of interest (ROI) matching the size of the spots (fig. 3.3) for each z plane. I then obtained a z-intensity profile which I fitted with a Gaussian (for the case without TF) or a Lorentzian (for the case with TF) function. For each fit, I calculated its FWHM. This was repeated for different spot sizes. As expected, TF significantly improves axial resolution. Fig. 3.4 shows a linear dependence between the spot diameter and axial resolution for CGH in absence of TF, while with TF the resolution remains at a constant value of 11.0 ± 0.2 um; this corresponds to theoretical considerations [77, 50]. For dense biological samples that have a lot of cells on

top of each other, using TF is thus necessary to illuminate single cells and reduce noise from the other planes.

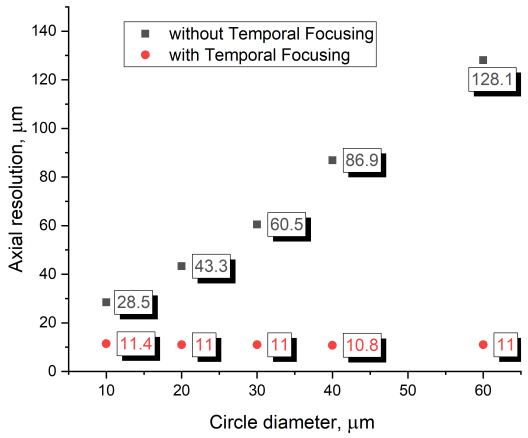

Figure 3.4: Plot of the axial resolution for different circle diameters. Labels are the resolution values in um.

My next goal was to analyse the diffraction efficiency of the set-up. For a holographic spot with coordinates x, y the diffraction efficiency is defined as the ratio of intensities $I(x,y)/I(0,0)$, with $I(0,0)$ being the intensity of the zeroth order [84] . Following the laws of diffraction optics, after a rectangular aperture the intensity will have this distribution [54]:

$$\begin{aligned} \frac{I(x,y)}{I(0,0)} &= \left(\frac{\sin X}{X}\right)^2 \left(\frac{\sin Y}{Y}\right)^2, \\ X = \frac{m\pi a}{\lambda f}x, &\quad Y = \frac{m\pi a}{\lambda f}y, \end{aligned} \tag{3.1}$$

where m is the refractive index at the sample plane, a is the size of a SLM pixel at the back focal plane of the objective, λ is the light wavelength, and f is the focal length of the objective. In our system, $m = 1.33$, $a = 20$ um, $\lambda = 1030$ nm, and $f = 8.5$ mm; with these values we can plot the theoretical diffraction efficiency.

To measure it experimentally, we need to create holographic spots for all x, y coordinates and record their intensity. I chose a spot with a 30 um diameter, this way they can be space out across the field of view. A combined image of

experimental spots is shown in fig. 3.5a.

So, in fig. 3.5c and 3.5b are presented two plots showing the theoretical and experimental diffraction efficiency. They are similar, with the theoretical FWHM being 297±4 um, and the experimental one 225±17 um. The latter is not perfectly circular, this probably has to do that the SLM is rectangular. It also has got a strong background signal. Clearly, the intensity is strongest in the centre, and starts dropping quickly after 100 um in any direction. An experimenter has to keep this in mind when creating holograms of a large size: the cells far away from the centre might not get enough energy to be excited.

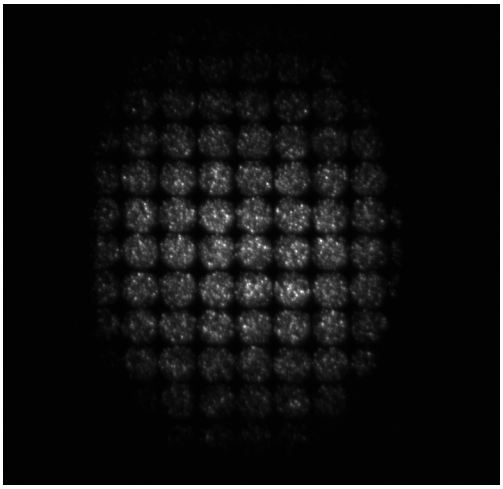

(a) A collage of spots for measuring the diffraction efficiency. Each spot has a diameter of 30 um, and the picture size is 370x370 um.

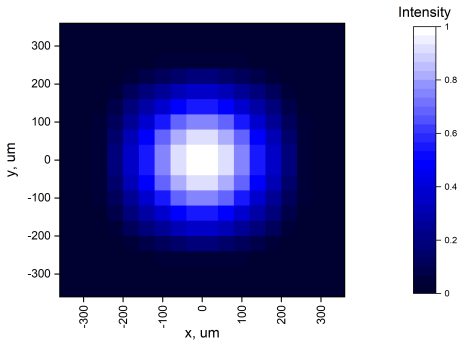

(b) Theoretical result following formula 3.1.

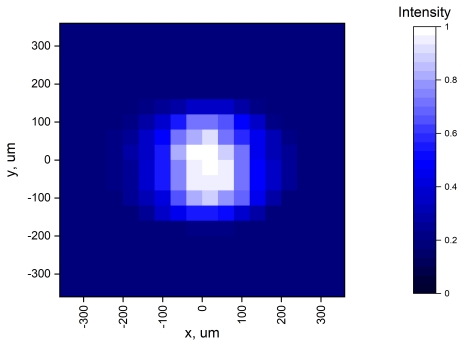

(c) Experimental result plotted from the averaged intensities of the fig. 3.5a.

Figure 3.5: Comparison of theoretical and experimental diffraction efficiency maps for the holography system.

Finally, 2p Ca images of a patch of opsin expressing neurons are presented in fig. 3.6; the bright pattern of stimulation is clearly visible in the selected cells. The pictures themselves were acquired with dual-galvo scanning, averaged across 50 frames (10 s of recording). The scanning resolution is 0.7 um in the xy plane, making it more than enough to distinguish different cells. Live neurons produce a natural activity pattern, which explains the faint image we see before the stimulation. After it, the cells emit a bright fluorescent signal, and then return to their baseline in around one minute. The standard values for the stimulation parameters in CGH beam are 20 mW, 50 ms per cell. With the maximum power of the set-up at 1 W, we could stimulate up to 50 cells at the same time.

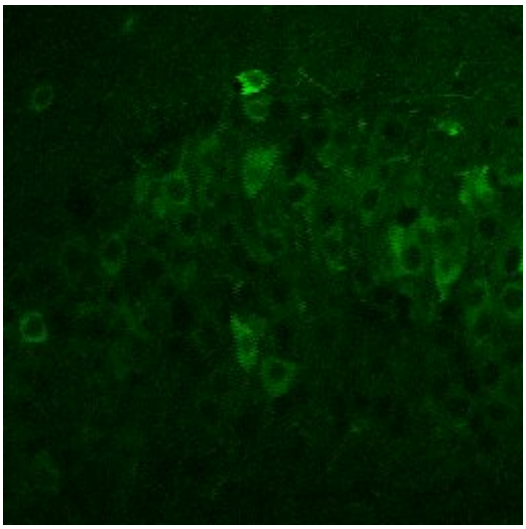

(a) Average of 50 frames of background neuron activity.

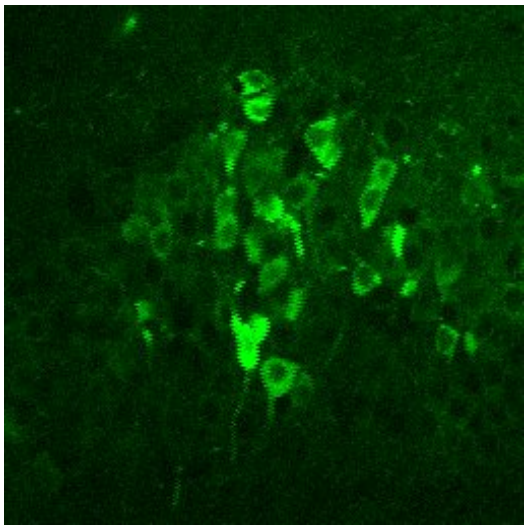

(b) Average of 50 frames after cell stimulation.

Figure 3.6: Calcium images of a patch of opsin expressing neurons before and after stimulation with CGH. The field of view is 450x450 um.

3.3 DMD integration

In the next step, I integrated a digital micromirror device (DMD) into the system.

DMD is useful in the experiments that aim to establish normal retina functionality under visible light. The pattern of light is projected onto the photoreceptors of a healthy retina, and the signal of the ganglion cells is analysed for different patterns. DMD provides complex pattern sequences that can be updated in real

time. My goal was to create patterns across 1x1 mm area at 30 Hz to illuminate the whole fovea.

The optical path is presented in detail in fig. 3.7. It consists of an LED, a collimator system, the DMD, and then a lens ($f_3 = 200$ mm) and an objective ($f_4 = 18$ mm) in a $4f$ configuration. This way, the total magnification of the system is f_4/f_3 , which is equal to -0.09. This means that the active area of the DMD of 14x10.5 mm transforms into 1.26x0.945 mm field of view in the object plane. The DMD chip need to be set at the focal plane of L3. To align it, a small auxiliary laser is placed perpendicular to the dichroic mirror, and its beam is centred on the DMD chip, at the distance of f_3. After that, the DMD is turned on, and the pattern (a spinning wheel in this case) is reflected at around 12°, and that path is then centred using the camera image. Finally, to make sure the focal plane of the DMD light path coincides with the focal plane of the imaging part, I had to adjust the substage platform with the objective.

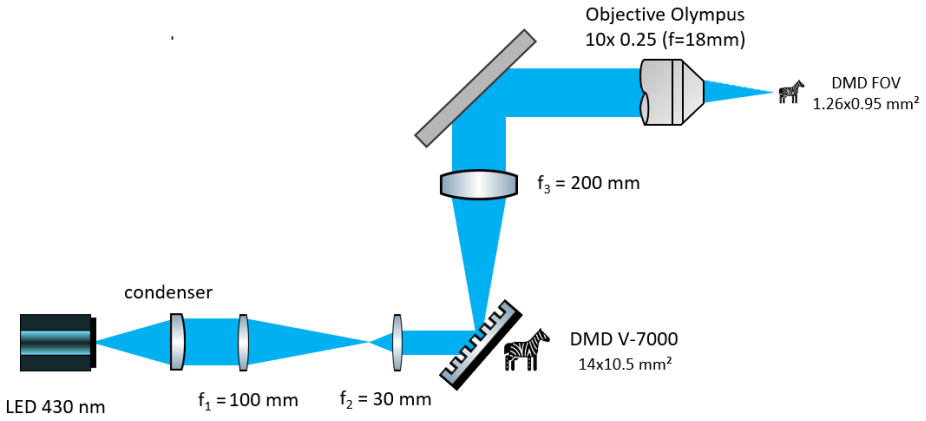

Figure 3.7: Optical path of the DMD set-up.

Integrating the DMD with the rest of the set-up required to make a suitable user interface for it. To do that, I used a Python based API called ALP4lib [85] that communicates with the DMD via ALP4.1 driver. My interface (see fig. 3.8a) allowed for updates in real-time, including: user drawing, creating patterns, extracting pixel positions, uploading sequences, and playing basic animations.

With the interface complete, I performed calibration tests using the whole set-up with the DMD. After adjustments that made the DMD-patterned light visible

on the sample, I used a microruler slide with a unit cell of 50 um. I set the positions of several points using the interface, and then, with the widefield CCD camera I measured their position and distances between them. The values matched with the theoretical calculations described above. For a single micromirror pitch (size) of 13.7 um, its image on the sample is 1.2 um. This is well below typical cell sizes and therefore is satisfactory for the experiments.

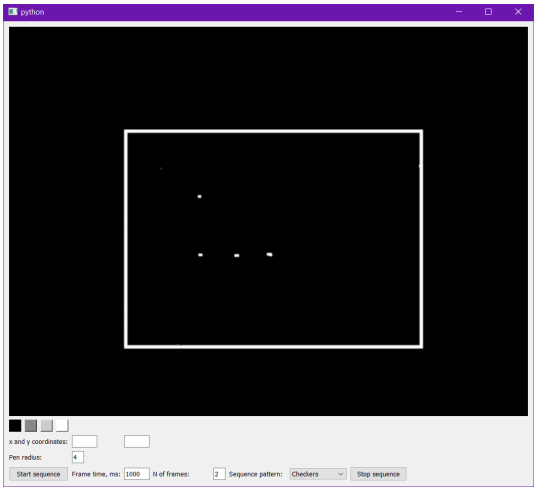

(a) A screenshot of the custom-built DMD interface. The white rectangle roughly corresponds to the initial field of view for the magnification used.

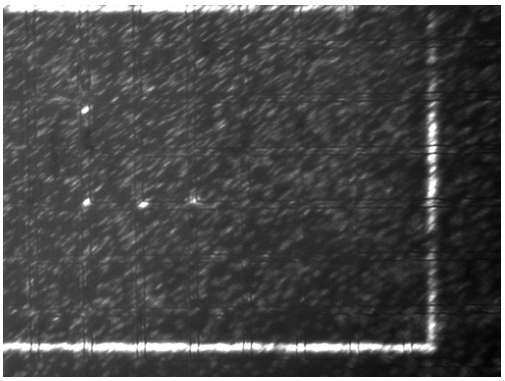

(b) The pattern of light as seen by the camera. The contrast was adjusted for better visibility of the ruler. The points correspond to the ones drawn on the computer.

Figure 3.8: DMD calibration.

3.4 Fixational eye movements

Fixational movements are discussed in the section 1.2. These movements are larger than typical retinal cell size, so to precisely stimulate single cells with holography techniques in living eyes, we would need to track this motion and adjust for it in real time. This applies only to prospective live experiments, but that is the end goal of the overall project.

A confocal scanning laser ophthalmoscope is a standard tool [86, 87] to collect images of the retina with a spatial resolution on the order of several um [88]. Recorded images are compared to a reference frame in order to obtain the translational shift between them. The challenge is to do it in real time, and one solution

that we plan to use in the future is to record subsampled (partially black) images and to do a fast cross-correlation analysis to measure the shift [89].

However, the current goal of the project is to develop an algorithm that would allow to move the holographic pattern on the retina along with the fixational eye movements. Since the pattern is created via a phase modulation (SLM, described in section 2.3.2), it uses a Fourier transform. We need a quick way to laterally shift the pattern without recalculating the SLM phase mask from the beginning, since it takes time and might lead to lagging behind the actual eye movements.

Fourier transform offers its argument shifting property to recalculate the phase for a shifted image:

$$\begin{gathered} x(n) \overset{FT}{\Leftrightarrow} X(\omega) \\ x(n-k) \overset{FT}{\Leftrightarrow} \exp(-i\omega k) X(\omega) \end{gathered} \tag{3.2}$$

To implement the formula 3.2, I needed to know the spatial frequencies used in FFT function. For a image window of length n and a sample spacing d, they range from $-\frac{1}{2d}$ to $\frac{1}{2d}$ with a step of $\frac{1}{dn}$ as defined by the Nyquist theorem [90]. In Python FFT implementation, they are arranged into an array as follows [91]:

$$\begin{aligned} f &= \left[0, 1, ..., \frac{n}{2} - 1, -\frac{n}{2}, ..., -1\right] / dn, \quad \text{for even } n; \\ f &= \left[0, 1, ..., \frac{n-1}{2} - 1, -\frac{n-1}{2}, ..., -1\right] / dn, \quad \text{for odd } n. \end{aligned} \tag{3.3}$$

To reproduce the fixational movement, I tracked cell movement using ImageJ in a live recording from a healthy young volunteer. The trajectories of three selected cells are presented in fig. 3.9a: you can see the last frame of the video with highlighted tracks. The analysed part of the recording was shot at 30 Hz and lasted for 3 s. Most of the time the cells jiggle randomly in the same place with a small amplitude (tremor and drift), and then they make several long-distance jumps, similar across all the three cells. The usual amplitude of tremor and drift is 50 um, while the microsaccade jumps are around 100 um — this matches with values found in other work [13].

Using an FFT Python implementation, I wrote a program that shifts an image along a given trajectory. As an illustration, let us imagine that we are trying to project an image of a small square onto the retina. The GS algorithm calculates

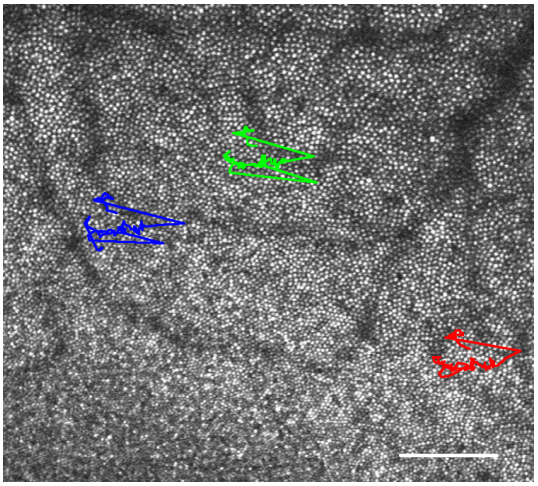

(a) Image of the retinal photoreceptors. Three cell trajectories are shown as accumulating lines during 3 seconds of fixational movement. Scale bar is 100 um.

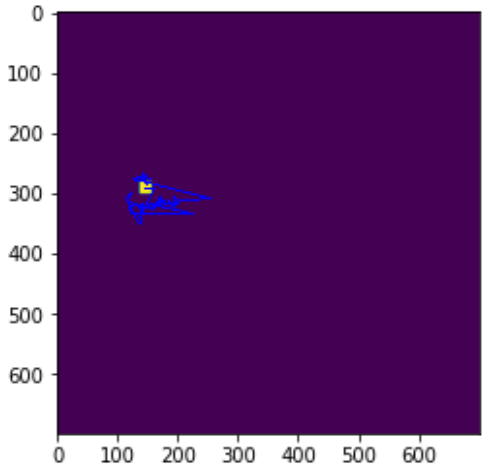

(b) Output of the Python program with the accumulated trajectory of the square set to follow the first cell from the retina recording.

Figure 3.9: Fixational movement tracking results.

the appropriate phase mask for the SLM, and then the eye moves like in the live recording discussed above. Using the FT time shift property, my program recalculates the phase mask, and then takes an IFFT to plot the resulting image. Fig. 3.9b shows a square precisely repeating the cell's fixational movement tracked from the recording.

Unfortunately, the current computational time for the new phase masks exceeds the time for one frame, therefore, it lags behind. Between some frames the movement is too small to compensate, so we can reasonably reduce the mask refreshment rate. Another parameter defining computation speed is the image resolution. Just by regulating these two factors, a 150x150 image can be shifted at 15 Hz, good enough to keep up with every second frame of the recording. This is still not a great result, and future improvement involves rewriting the program in C instead of Python and optimising the calculation.

I was also considering different approaches: for example, using a linear FT property and calculating a FT of the difference between the start and end square positions. This approach is much faster, but unfortunately it doesn't work with GS algorithm, since it asks to modify both the phase and the phase of the incoming beam.

Another potential problem to resolve is the looping character of the FT: if our square were to jump a long distance to the left, it would appear at the right border of the image. Obviously, this is not the case for microsaccades in the real eye, so we will have to keep track of the real borders of our field of view.

Conclusion

In the course of this master thesis I worked closely with a computer generated holography set-up, and I measured its axial resolution and diffraction efficiency. I successfully integrated a light modulating device, DMD, into the set-up and created a Python interface for it, which allows for real-time control and sequence display. Finally, I studied the fixational eye movement and made a program to compensate for them using FT as a basis for future integration into the SLM phase mask calculating algorithm.

The set-up is not without several limitations. An important experimental feature, which currently cannot be done, is the ability to create a 3D hologram pattern to target cells in different planes. It can be achieved with multiplexed 3D-CGH methods [92, 93], which require a second SLM installed on the set-up. Another potential problem is the lack of precise synchronisation between the DMD and the imaging system: to study fast cell response it is vital to know the exact moment of illumination.

This work is a part of a larger project on holographic vision restoration, which will be the subject of my PhD research. It will involve using the CGH set-up to study connections between retinal layers on real samples (mice and primates), and then to transfer this knowledge into optogenetic blindness therapy solutions. Optogenetic treatment is a novel and complex approach; and currently, only four groups are registered early phase clinical trials in retinal degeneration patients [94]. Many practical challenges need to be overcome: the timing of the treatment, choice of an optimal opsin, toxicity, potential long-term effects, and efficiency. And here every step towards a working treatment is a step to creating a better future.

Bibliography

[1] S. R. Flaxman, R. R. Bourne, S. Resnikoff, P. Ackland, T. Braithwaite, M. V. Cicinelli, A. Das, J. B. Jonas, J. Keeffe, J. H. Kempen, *et al.*, "Global causes of blindness and distance vision impairment 1990–2020: a systematic review and meta-analysis," *The Lancet Global Health*, vol. 5, no. 12, pp. e1221–e1234, 2017.

[2] S. Sridharan, M. A. Gajowa, M. B. Ogando, U. K. Jagadisan, L. Abdeladim, M. Sadahiro, H. A. Bounds, W. D. Hendricks, T. S. Turney, I. Tayler, *et al.*, "High-performance microbial opsins for spatially and temporally precise perturbations of large neuronal networks," *Neuron*, vol. 110, no. 7, pp. 1139–1155, 2022.

[3] P. Artal, *Handbook of visual optics, two-volume set*. CRC Press, 2017.

[4] G. Wald, *The vertebrate eye and its adaptive radiation*, ch. 8. Bloomfield Hills, Mich., Cranbrook Institute of Science, 1944.

[5] H.-J. Wagner, R. H. Douglas, T. M. Frank, N. W. Roberts, and J. C. Partridge, "A novel vertebrate eye using both refractive and reflective optics," *Current Biology*, vol. 19, no. 2, pp. 108–114, 2009.

[6] D. A. Atchison, G. Smith, and G. Smith, *Optics of the human eye*, vol. 35. Butterworth-Heinemann Oxford, 2000.

[7] D. Purves, G. J. Augustine, D. Fitzpatrick, L. C. Katz, A.-S. LaMantia, J. O. McNamara, S. M. Williams, *et al.*, "Types of eye movements and their functions," *Neuroscience*, vol. 20, pp. 361–390, 2001.

[8] B. Farnsworth, "Types of eye movements [Saccades and Beyond]," 2019.

[9] A. A. McCall, D. M. Miller, and B. J. Yates, "Descending influences on vestibulospinal and vestibulosympathetic reflexes," *Frontiers in neurology*, vol. 8, p. 112, 2017.

[10] A. G. Feldman and L. Zhang, "Eye and head movements and vestibulo-ocular reflex in the context of indirect, referent control of motor actions," *Journal of Neurophysiology*, vol. 124, no. 1, pp. 115–133, 2020.

[11] D. H. Hubel and T. N. Wiesel, "Receptive fields and functional architecture in two nonstriate visual areas (18 and 19) of the cat," *Journal of neurophysiology*, vol. 28, no. 2, pp. 229–289, 1965.

[12] R. G. Alexander and S. Martinez-Conde, "Fixational eye movements," *Eye Movement Research*, pp. 73–115, 2019.

[13] S. Martinez-Conde, S. L. Macknik, and D. H. Hubel, "The role of fixational eye movements in visual perception," *Nature reviews neuroscience*, vol. 5, no. 3, pp. 229–240, 2004.

[14] A. L. Yarbus, *Eye movements and vision*. Springer, 2013.

[15] F. Ratliff and L. A. Riggs, "Involuntary motions of the eye during monocular fixation.," *Journal of experimental psychology*, vol. 40, no. 6, p. 687, 1950.

[16] R. M. Pritchard, "Stabilized images on the retina," *Scientific American*, vol. 204, no. 6, pp. 72–79, 1961.

[17] R. J. Leigh and D. S. Zee, *The neurology of eye movements*. Contemporary Neurology, 2015.

[18] R. Leigh and D. S. Zee, "Eye movements of the blind," *Investigative Ophthalmology & Visual Science*, vol. 19, no. 3, pp. 328–331, 1980.

[19] C. P. Wilkinson, D. R. Hinton, S. R. Sadda, and P. Wiedemann, *Ryan's Retina*. Elsevier Health Sciences, 2017.

[20] P. Ahnelt, "The photoreceptor mosaic," *Eye*, vol. 12, no. 3, pp. 531–540, 1998.

[21] A. Roorda, A. B. Metha, P. Lennie, and D. R. Williams, "Packing arrangement of the three cone classes in primate retina," *Vision research*, vol. 41, no. 10-11, pp. 1291–1306, 2001.

[22] J. Hurley, "Phototransduction," *Encyclopedia of Neuroscience*, pp. 687–692, 2009.

[23] "The nobel prize in physiology or medicine 1967."

[24] S. Barnes and M. E. Kelly, "Calcium channels at the photoreceptor synapse," *Photoreceptors and calcium*, pp. 465–476, 2002.

[25] X. Ling, E. H. Silson, and R. D. McIntosh, "Did you see it? a python tool for psychophysical assessment of the human blind spot," *PloS one*, vol. 16, no. 11, p. e0254195, 2021.

[26] A. Bringmann, S. Syrbe, K. Görner, J. Kacza, M. Francke, P. Wiedemann, and A. Reichenbach, "The primate fovea: structure, function and development," *Progress in retinal and eye research*, vol. 66, pp. 49–84, 2018.

[27] G. Staurenghi, S. Sadda, U. Chakravarthy, R. F. Spaide, *et al.*, "Proposed lexicon for anatomic landmarks in normal posterior segment spectral-domain optical coherence tomography: the IN-OCT consensus," *Ophthalmology*, vol. 121, no. 8, pp. 1572–1578, 2014.

[28] R. G. Alexander, R. J. Mintz, P. J. Custodio, S. L. Macknik, A. Vaziri, A. Venkatakrishnan, S. Gindina, and S. Martinez-Conde, "Gaze mechanisms enabling the detection of faint stars in the night sky," *European Journal of Neuroscience*, vol. 54, no. 4, pp. 5357–5367, 2021.

[29] L. A. Remington and D. Goodwin, *Clinical Anatomy and Physiology of the Visual System E-Book*. Elsevier Health Sciences, 2021.

[30] S. Tom Dieck, W. D. Altrock, M. M. Kessels, B. Qualmann, H. Regus, D. Brauner, A. Fejtová, O. Bracko, E. D. Gundelfinger, and J. H. Brandstatter, "Molecular dissection of the photoreceptor ribbon synapse: physical interaction of bassoon and ribeye is essential for the assembly of the ribbon complex," *The Journal of cell biology*, vol. 168, no. 5, pp. 825–836, 2005.

[31] S. H. DeVries, W. Li, and S. Saszik, "Parallel processing in two transmitter microenvironments at the cone photoreceptor synapse," *Neuron*, vol. 50, no. 5, pp. 735–748, 2006.

[32] U. Grunert and P. R. Martin, "Rod bipolar cells in the macaque monkey retina: immunoreactivity and connectivity," *Journal of Neuroscience*, vol. 11, no. 9, pp. 2742–2758, 1991.

[33] S. V. O. Lameirao, D. E. Hamassaki, A. R. Rodrigues, S. M. A. De Lima, B. L. Finlay, and L. C. L. Silveira, "Rod bipolar cells in the retina of the capuchin monkey (cebus apella): characterization and distribution," *Visual Neuroscience*, vol. 26, no. 4, pp. 389–396, 2009.

[34] P. R. Martin and U. Grünert, "Spatial density and immunoreactivity of bipolar cells in the macaque monkey retina," *Journal of Comparative Neurology*, vol. 323, no. 2, pp. 269–287, 1992.

[35] R. G. Smith, M. A. Freed, and P. Sterling, "Microcircuitry of the dark-adapted cat retina: functional architecture of the rod-cone network," *Journal of Neuroscience*, vol. 6, no. 12, pp. 3505–3517, 1986.

[36] C. Hamel, "Retinitis pigmentosa," *Orphanet journal of rare diseases*, vol. 1, no. 1, pp. 1–12, 2006.

[37] "Retinitis Pigmentosa | National Eye Institute."

[38] D. T. Hartong, E. L. Berson, and T. P. Dryja, "Retinitis pigmentosa," *The Lancet*, vol. 368, no. 9549, pp. 1795–1809, 2006.

[39] P. A. Campochiaro and T. A. Mir, "The mechanism of cone cell death in retinitis pigmentosa," *Progress in retinal and eye research*, vol. 62, pp. 24–37, 2018.

[40] W. Yan, P. Long, D. Wei, W. Yan, X. Zheng, G. Chen, J. Wang, Z. Zhang, T. Chen, and M. Chen, "Protection of retinal function and morphology in MNU-induced retinitis pigmentosa rats by ALDH2: An in-vivo study," *BMC ophthalmology*, vol. 20, no. 1, pp. 1–10, 2020.

[41] E. S. Boyden, F. Zhang, E. Bamberg, G. Nagel, and K. Deisseroth, "Millisecond-timescale, genetically targeted optical control of neural activity," *Nature neuroscience*, vol. 8, no. 9, pp. 1263–1268, 2005.

[42] D. Wang, P. W. Tai, and G. Gao, "Adeno-associated virus vector as a platform for gene therapy delivery," *Nature reviews Drug discovery*, vol. 18, no. 5, pp. 358–378, 2019.

[43] G. Nagel, T. Szellas, W. Huhn, S. Kateriya, N. Adeishvili, P. Berthold, D. Ollig, P. Hegemann, and E. Bamberg, "Channelrhodopsin-2, a directly light-gated cation-selective membrane channel," *Proceedings of the National Academy of Sciences*, vol. 100, no. 24, pp. 13940–13945, 2003.

[44] E. G. Govorunova, E. N. Spudich, C. E. Lane, O. A. Sineshchekov, and J. L. Spudich, "New channelrhodopsin with a red-shifted spectrum and rapid kinetics from Mesostigma viride," *MBio*, vol. 2, no. 3, pp. e00115–11, 2011.

[45] F. Zhang, L.-P. Wang, E. S. Boyden, and K. Deisseroth, "Channelrhodopsin-2 and optical control of excitable cells," *Nature methods*, vol. 3, no. 10, pp. 785–792, 2006.

[46] V. Emiliani, A. E. Cohen, K. Deisseroth, and M. Häusser, "All-optical interrogation of neural circuits," *Journal of Neuroscience*, vol. 35, no. 41, pp. 13917–13926, 2015.

[47] R. A. de Melo Reis, H. R. Freitas, and F. G. De Mello, "Cell calcium imaging as a reliable method to study neuron–glial circuits," *Frontiers in Neuroscience*, vol. 14, p. 569361, 2020.

[48] E. Carafoli and J. Krebs, "Why calcium? How calcium became the best communicator," *Journal of Biological Chemistry*, vol. 291, no. 40, pp. 20849–20857, 2016.

[49] J.-A. Sahel, E. Boulanger-Scemama, C. Pagot, A. Arleo, F. Galluppi, J. N. Martel, S. D. Esposti, A. Delaux, J.-B. de Saint Aubert, C. de Montleau, *et al.*, "Partial recovery of visual function in a blind patient after optogenetic therapy," *Nature Medicine*, vol. 27, no. 7, pp. 1223–1229, 2021.

[50] E. Ronzitti, C. Ventalon, M. Canepari, B. C. Forget, E. Papagiakoumou, and V. Emiliani, "Recent advances in patterned photostimulation for optogenetics," *Journal of Optics*, vol. 19, no. 11, p. 113001, 2017. Publisher: IOP Publishing.

[51] E. Papagiakoumou, E. Ronzitti, and V. Emiliani, "Scanless two-photon excitation with temporal focusing," *Nature Methods*, vol. 17, no. 6, pp. 571–581, 2020.

[52] J. J. Nassi and E. M. Callaway, "Parallel processing strategies of the primate visual system," *Nature reviews neuroscience*, vol. 10, no. 5, pp. 360–372, 2009.

[53] G. F. Marshall and G. E. Stutz, *Handbook of optical and laser scanning*. Taylor & Francis, 2012.

[54] M. Born and E. Wolf, *Principles of optics*. Cambridge University Press, 1997.

[55] L. Petreanu, T. Mao, S. M. Sternson, and K. Svoboda, "The subcellular organization of neocortical excitatory connections," *Nature*, vol. 457, no. 7233, pp. 1142–1145, 2009.

[56] N. L. Rochefort, M. Narushima, C. Grienberger, N. Marandi, D. N. Hill, and A. Konnerth, "Development of direction selectivity in mouse cortical neurons," *Neuron*, vol. 71, no. 3, pp. 425–432, 2011.

[57] K. Nadella, H. Roš, C. Baragli, V. A. Griffiths, G. Konstantinou, T. Koimtzis, G. J. Evans, P. A. Kirkby, and R. A. Silver, "Random-access scanning microscopy for 3D imaging in awake behaving animals," *Nature methods*, vol. 13, no. 12, pp. 1001–1004, 2016.

[58] T. Raj, F. H. Hashim, A. B. Huddin, M. F. Ibrahim, and A. Hussain, "A survey on lidar scanning mechanisms," *Electronics*, vol. 9, no. 5, p. 741, 2020.

[59] N. Savage, "Acousto-optic devices," *Nature photonics*, vol. 4, no. 10, pp. 728–729, 2010.

[60] J. Sapriel, V. Y. Molchanov, G. Aubin, and S. Gosselin, "Acousto-optic switch for telecommunication networks," in *Acousto-Optics and Applications V*, vol. 5828, pp. 68–75, SPIE, 2005.

[61] E. Chaigneau, E. Ronzitti, M. A. Gajowa, G. J. Soler-Llavina, D. Tanese, A. Y. Brureau, E. Papagiakoumou, H. Zeng, and V. Emiliani, "Two-photon holographic stimulation of ReaChR," *Frontiers in Cellular Neuroscience*, vol. 10, p. 234, 2016.

[62] A. Bègue, E. Papagiakoumou, B. Leshem, R. Conti, L. Enke, D. Oron, and V. Emiliani, "Two-photon excitation in scattering media by spatiotemporally shaped beams and their application in optogenetic stimulation," *Biomedical optics express*, vol. 4, no. 12, pp. 2869–2879, 2013.

[63] G. Faini, C. Molinier, C. Telliez, C. Tourain, B. C. Forget, E. Ronzitti, and V. Emiliani, "Ultrafast light targeting for high-throughput precise control of neuronal networks," *Biorxiv*, 2021.

[64] N. Grossman, V. Poher, M. S. Grubb, G. T. Kennedy, K. Nikolic, B. McGovern, R. B. Palmini, Z. Gong, E. M. Drakakis, M. A. Neil, *et al.*, "Multi-site optical excitation using ChR2 and micro-LED array," *Journal of neural engineering*, vol. 7, no. 1, p. 016004, 2010.

[65] G. ViALUX, "SuperSpeed specification."

[66] A. Bhatia, S. Moza, and U. S. Bhalla, "Patterned optogenetic stimulation using a dmd projector," in *Channelrhodopsin*, pp. 173–188, Springer, 2021.

[67] F. Anselmi, A. Banerjee, and D. F. Albeanu, "Patterned photostimulation in the brain," in *New Techniques in Systems Neuroscience*, pp. 235–270, Springer, 2015.

[68] J. W. Goodman, *Introduction to Fourier Optics*. Roberts and Company Publishers, 2005. Google-Books-ID: ow5xs_Rtt9AC.

[69] F. Benfenati, E. Di Fabrizio, and V. Torre, *Novel Approaches for Single Molecule Activation and Detection*, vol. 4. Springer, 2014.

[70] O. Tzang, E. Niv, S. Singh, S. Labouesse, G. Myatt, and R. Piestun, "Wavefront shaping in complex media with a 350 kHz modulator via a 1D-to-2D transform," *Nature Photonics*, vol. 13, no. 11, pp. 788–793, 2019.

[71] P. Collins, "Understanding the jargon of LCOS spatial light modulators (SLMs)."

[72] J. E. Curtis, B. A. Koss, and D. G. Grier, "Dynamic holographic optical tweezers," *Optics communications*, vol. 207, no. 1-6, pp. 169–175, 2002.

[73] H. J. Coufal, D. Psaltis, G. T. Sincerbox, *et al.*, *Holographic data storage*, vol. 8. Springer, 2000.

[74] R. Di Leonardo, F. Ianni, and G. Ruocco, "Computer generation of optimal holograms for optical trap arrays," *Optics Express*, vol. 15, no. 4, pp. 1913–1922, 2007.

[75] R. W. Gerchberg, "A practical algorithm for the determination of plane from image and diffraction pictures," *Optik*, vol. 35, no. 2, pp. 237–246, 1972.

[76] P. Chevalier, "Photonics laboratory: Spatial filtering and optical convolution," 2015.

[77] C. Lutz, T. S. Otis, V. DeSars, S. Charpak, D. A. DiGregorio, and V. Emiliani, "Holographic photolysis of caged neurotransmitters," *Nature methods*, vol. 5, no. 9, pp. 821–827, 2008.

[78] D. Oron, E. Tal, and Y. Silberberg, "Scanningless depth-resolved microscopy," *Optics express*, vol. 13, no. 5, pp. 1468–1476, 2005.

[79] E. Papagiakoumou, V. De Sars, D. Oron, and V. Emiliani, "Patterned two-photon illumination by spatiotemporal shaping of ultrashort pulses," *Optics Express*, vol. 16, no. 26, pp. 22039–22047, 2008.

[80] V. R. Curtis, N. W. Caira, J. Xu, A. G. Sata, and N. C. Pégard, "DCGH: Dynamic computer generated holography for speckle-free, high fidelity 3d displays," in *2021 IEEE Virtual Reality and 3D User Interfaces (VR)*, pp. 1–9, IEEE, 2021.

[81] B. Lee, D. Kim, S. Lee, C. Chen, and B. Lee, "High-contrast, speckle-free, true 3d holography via binary cgh optimization," *Scientific reports*, vol. 12, no. 1, pp. 1–12, 2022.

[82] R. Suda, M. Naruse, and R. Horisaki, "Incoherent computer-generated holography," *Optics Letters*, vol. 47, no. 15, pp. 3844–3847, 2022.

[83] Y. Mori, T. Fukuoka, and T. Nomura, "Speckle reduction in holographic projection by random pixel separation with time multiplexing," *Applied optics*, vol. 53, no. 35, pp. 8182–8188, 2014.

[84] S. Yang, E. Papagiakoumou, M. Guillon, V. De Sars, C.-M. Tang, and V. Emiliani, "Three-dimensional holographic photostimulation of the dendritic arbor," *Journal of neural engineering*, vol. 8, no. 4, p. 046002, 2011.

[85] S. M. Popoff, G. Shih, D. B, and Gustave Pariente, "wavefrontshaping/ALP4lib: 1.0.1."

[86] R. H. Webb and G. W. Hughes, "Scanning laser ophthalmoscope," *IEEE Transactions on Biomedical Engineering*, no. 7, pp. 488–492, 1981.

[87] R. H. Webb, G. W. Hughes, and F. C. Delori, "Confocal scanning laser ophthalmoscope," *Applied optics*, vol. 26, no. 8, pp. 1492–1499, 1987.

[88] O. Stachs, R. F. Guthoff, and S. Aumann, "In vivo confocal scanning laser microscopy," *High Resolution Imaging in Microscopy and Ophthalmology*, pp. 263–284, 2019.

[89] K. V. Vienola, M. Damodaran, B. Braaf, K. A. Vermeer, and J. F. de Boer, "In vivo retinal imaging for fixational eye motion detection using a high-speed digital micromirror device (DMD)-based ophthalmoscope," *Biomedical Optics Express*, vol. 9, no. 2, pp. 591–602, 2018.

[90] H. Landau, "Sampling, data transmission, and the Nyquist rate," *Proceedings of the IEEE*, vol. 55, no. 10, pp. 1701–1706, 1967.

[91] NumPy v1.23 Manual, "Numpy.fft.fftfreq function," 2022.

[92] N. Accanto, C. Molinier, D. Tanese, E. Ronzitti, Z. L. Newman, C. Wyart, E. Isacoff, E. Papagiakoumou, and V. Emiliani, "Multiplexed temporally focused light shaping for high-resolution multi-cell targeting," *Optica*, vol. 5, no. 11, pp. 1478–1491, 2018.

[93] N. C. Pégard, A. R. Mardinly, I. A. Oldenburg, S. Sridharan, L. Waller, and H. Adesnik, "Three-dimensional scanless holographic optogenetics with temporal focusing (3D-SHOT)," *Nature communications*, vol. 8, no. 1, pp. 1–14, 2017.

[94] M. Lindner, M. J. Gilhooley, S. Hughes, and M. W. Hankins, "Optogenetics for visual restoration: From proof of principle to translational challenges," *Progress in Retinal and Eye Research*, p. 101089, 2022.